Quantum Information Processing Summer School 2012

Hotel Beeze Bay Marina, Miyako, Japan August 12, 2012

Quantum Measurements

量子計測

Department of physics, Gakushuin University

学習院大学理学部物理学科

Takuya Hirano

平野　琢也

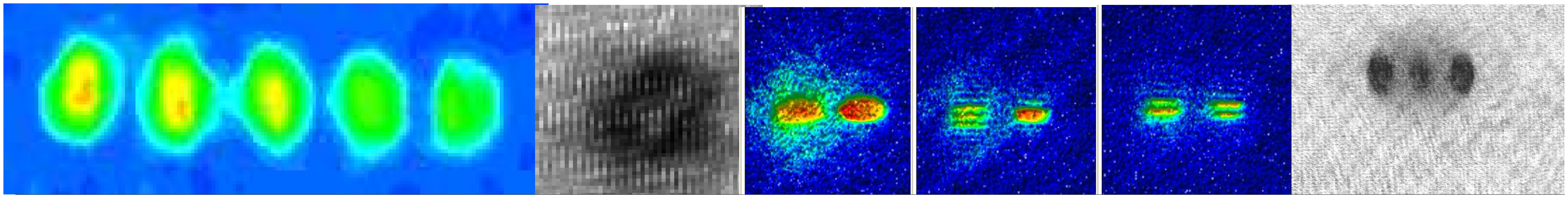

Self-introduction

１９８７年３月　東京大学理学部物理学科卒業　前半：塚田研究室，後半：清水忠雄研究室

１９８７年４月～１９９２年３月　東京大学物性研究所松岡研究室

　　　Ｍ１：超短パルス，CuCl中ポラリトン，Ｍ２－Ｄ３：パルス光スクイージング（町田さん）

１９９２年４月～１９９３年２月　日本学術振興会 特別研究員(PD)

　　　アンチバンチング（小芦さん）　連続量と離散量

１９９３年～１９９８年　東京大学久我研究室 助手

　　　LEDによるサブポアソン光の発生，レーザー冷却（重点領域でBEC，鳥井さん）

１９９８年～現在　　　学習院大学

　　　連続量の量子暗号，　Rb原子BEC，パルス光スクイージング

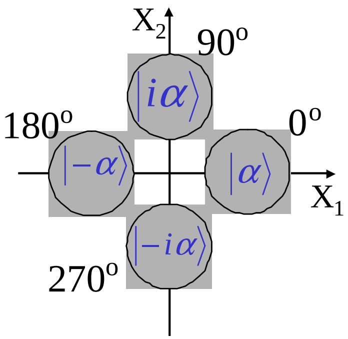

コヒーレント光通信

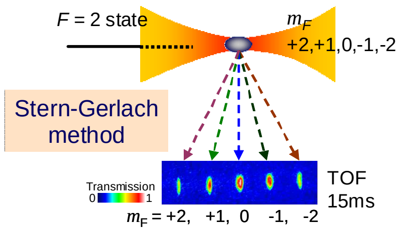

多成分凝縮体
→ 磁力計

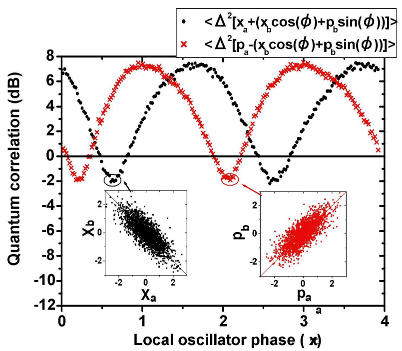

ループホールの無いEPR実験
通信への展開

Quantum Optics Group at Gakushuin

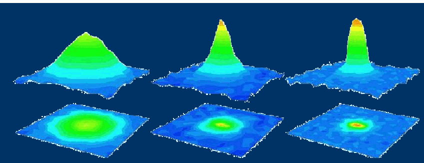

Prof. T. Hirano

Assist.Prof. S.Tojo → Chuo Univ. (2012/4/1～)

Assist.Prof. Y. Eto (2012/4/1～)

PostDoc. Mark Sadgrove → UEC (2012/7/16～)

PostDoc. T. Ichikawa (2012/4/1～)

Assist. H. Mori

M2 A. Koshio, S. Sekine

M1 Y. Koike, S. Togawa, Y. Tomiyama, S. Hasegawa, J. Miyazaki,

B4 A. Ohshiro, R. Matsuda, H. Ikeda, Y. Oguri, S. Kihara, H. Kogure, Y. Saito, S. Sato, H. Suzuki, N. Hashiyama M. Hata

Outline

1. Introduction
2. Magnetometer
3. Quantum enhanced measurements
4. Scaling
5. Conclusions

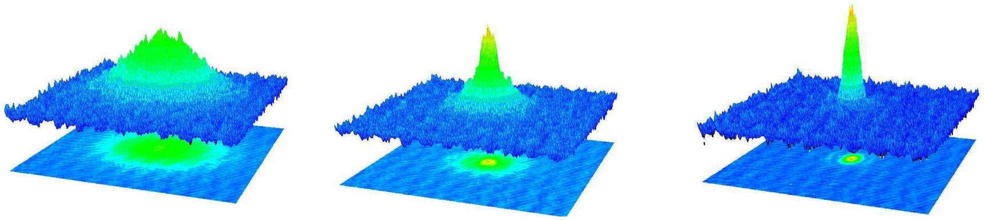

Introduction：量子計測とは

・FIRST量子情報処理プロジェクトのサブテーマ

・Terminology

量子計測

Quantum Measurements, Quantum Metrology, Quantum sensing

量子測定　　　　　　　　量子標準

・量子計測 ＝ 量子測定×応用（高精度測定）

従来よりも高精度・高感度の実現

スケーリング（少ないリソースによる高精度の実現）

→量子情報技術の有望な応用　　例：磁力計

Why magnetometer is important: Numerous and diverse applications

- **detection of magnetic field from brain and heart**

  non-invasive studies of individual cortical modules in the brain
- **detection of signals of NMR and MRI**
- **detection of microparticles**
- **detection of magnetic anomalies**

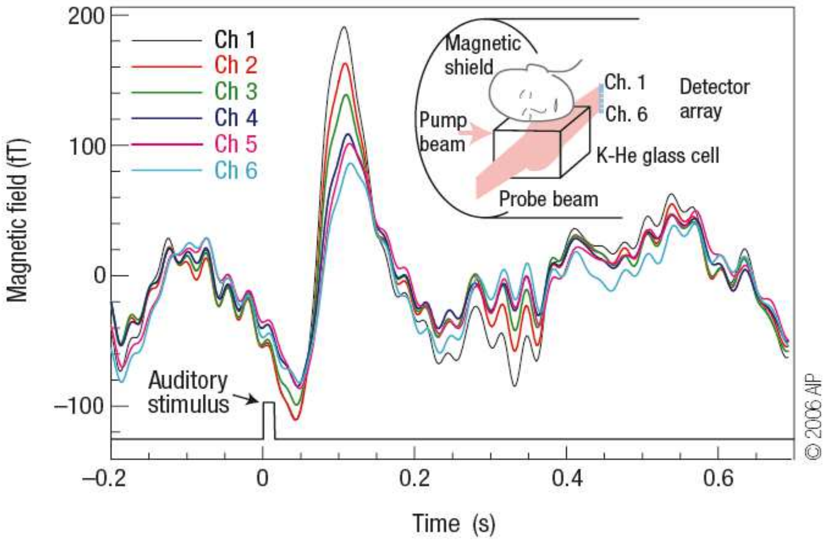

Magnetic fields recorded from a brain in response to an auditory stimulation by a series of short clicks (averaged over about 600 presentations). The prominent feature at 100 ms after the stimulus is the evoked response in the auditory cortex, most clearly seen as a difference in the magnetic fields recorded by different channels. In contrast, ambient field drifts, such as those seen before the stimulus, generate similar signals in all channels. (Xia, H., Baranga, A. B., Hoff man, D. & Romalis, M. V. Magnetoencephalography with an atomic magnetometer. Appl. Phys. Lett. 89, 211104 (2006).)

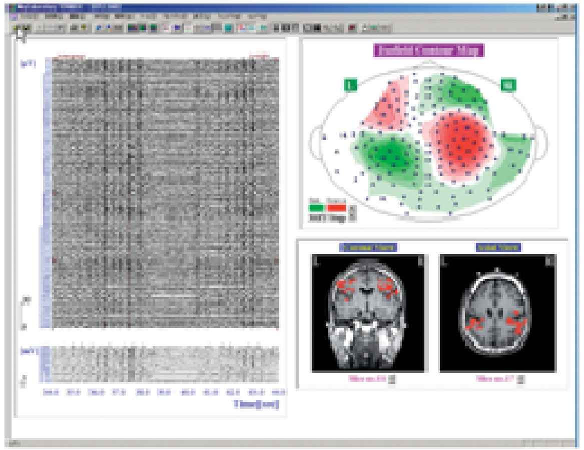

SQUID脳磁計（横河電機：MEGvision）

Magnetometer : present status

- Sensitivity of SQUID magneto-meters is approaching 10^{-15} T/√ Hz (with resolution of 1cm), but it is limited by 1/f noise at low frequencies.
- Kominis et al. demonstrated better than 10^{-15} T/√ Hz using atoms at room temperature:
  Nature **422**, 596 (2003).
- Cold atoms enables both high sensitivity and resolution:
  Nature 435, 440(2005); PRL 98, 200801(2007).
- Quantum control of atoms and light will enhance the sensitivity.
- High spatial resolution with NV center in diamond.

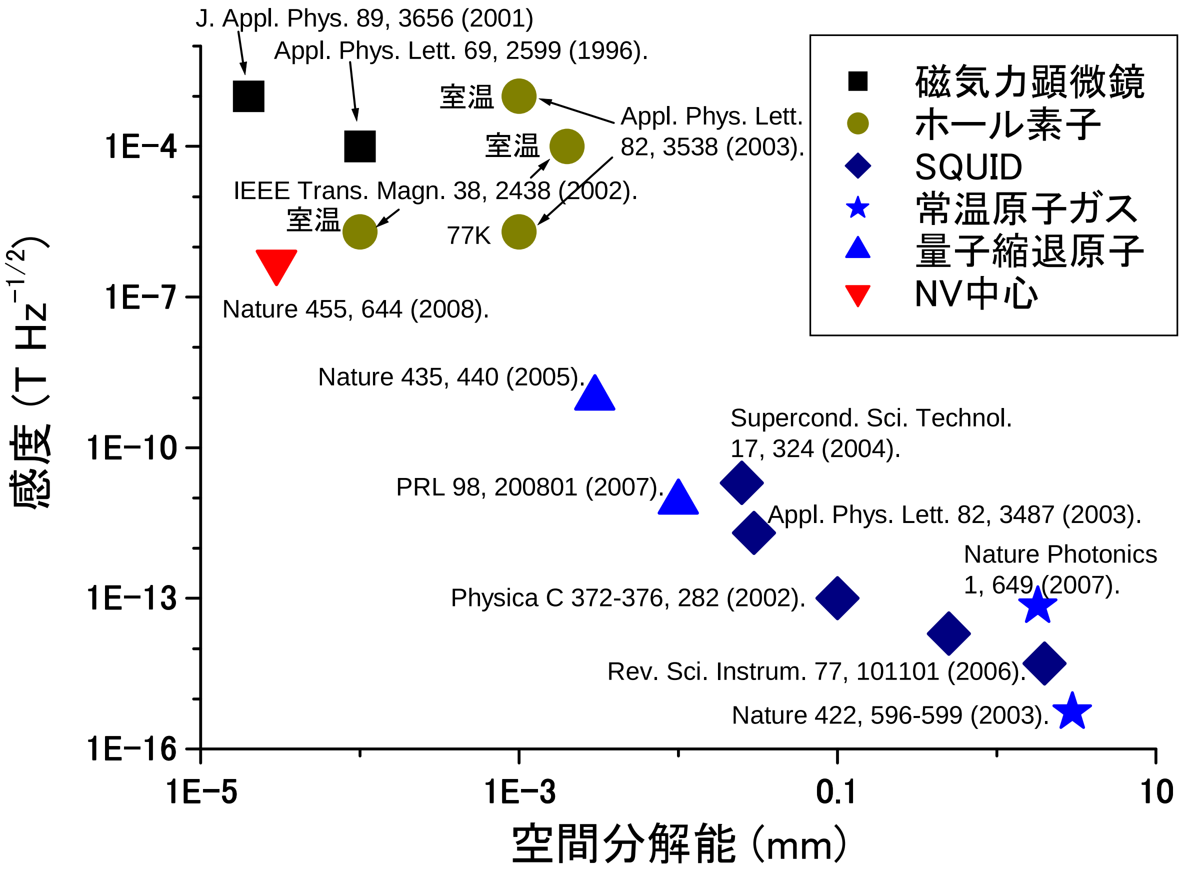

cf. Wildermuth et al., Nature 435, 440 (2005).

Optical Magnetometer

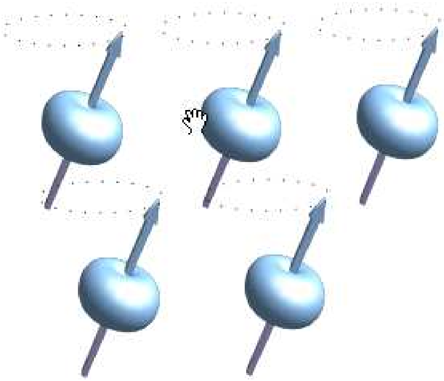

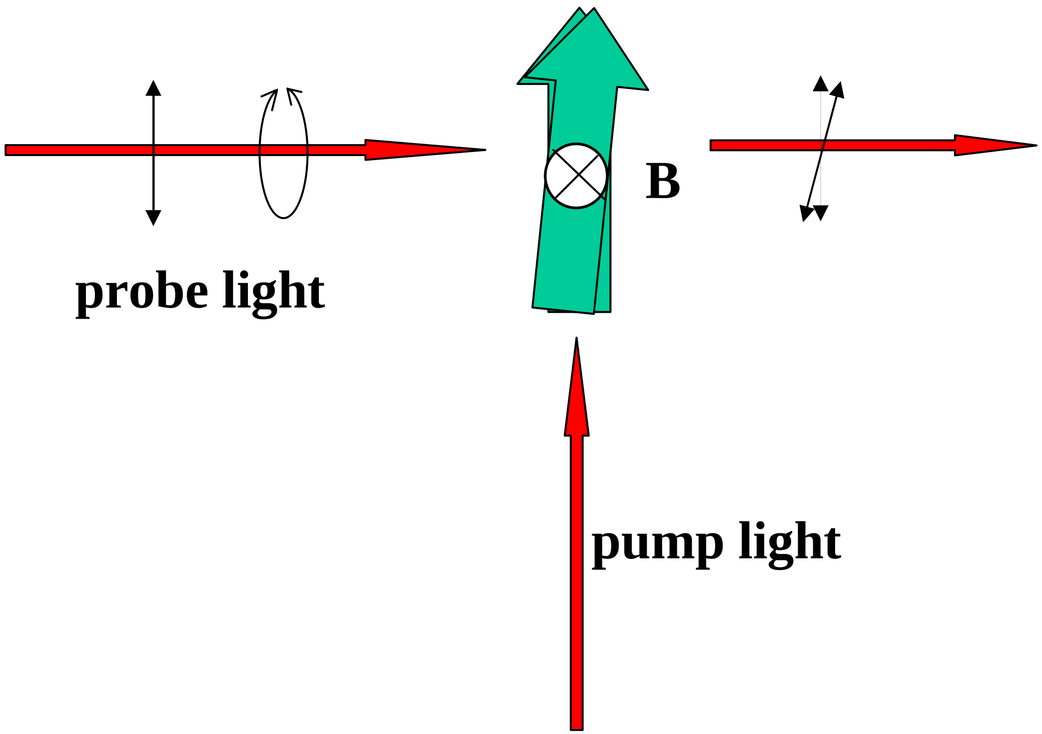

review article: D. Budker and M. Romalis, Nature Phys. 3, 227 (2007).

"A subfemtotesla multichannel atomic magnetometer,"

I. K. Kominis, T. W. Kornack, J. C. Allred & M. V. Romalis, Nature, Vol. 422, pp. 596-599 (2003).

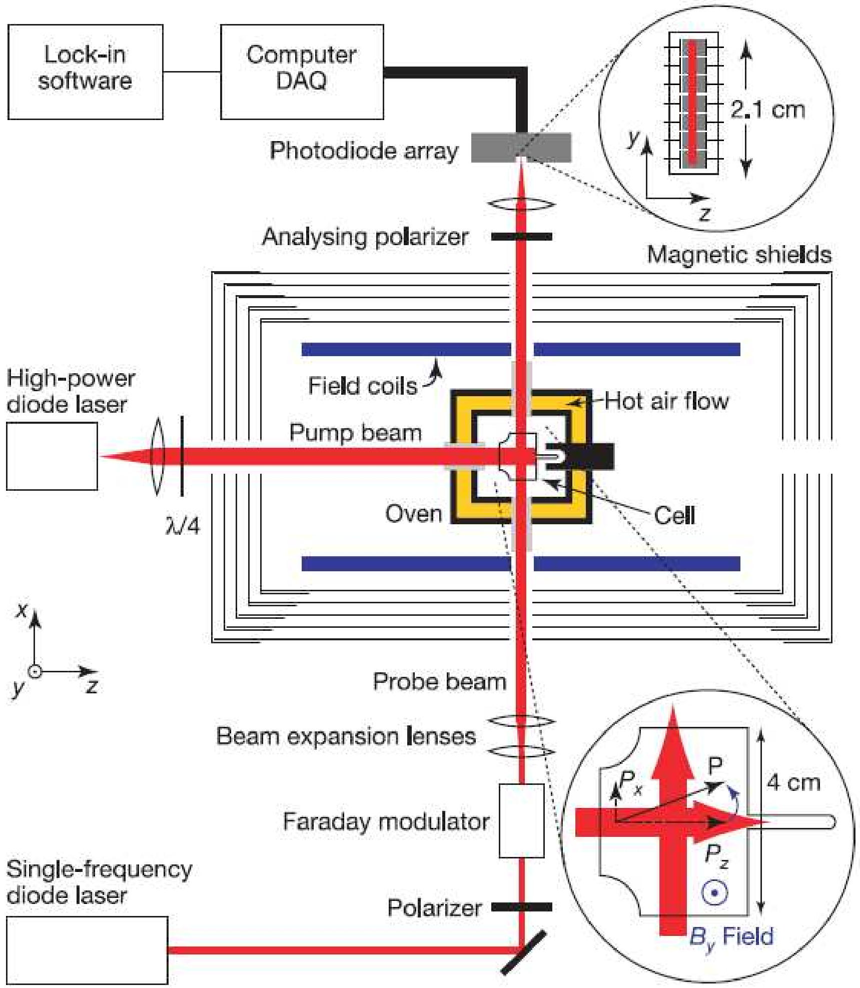

Figure 2 Experimental set-up. The diagram shows: magnetic shields with a shielding factor of 10^6; field coils producing calibrated, uniform fields along $\hat{x}$, $\hat{y}$ and $\hat{z}$ directions, and all five independent first-order field gradients; a T-shaped glass cell ($3 \times 4 \times 3$ cm) with flat windows, containing a drop of K metal, 2.9 atm of ^{4}He and 60 torr of N_2; a double-wall oven heated to 180 °C by flowing hot air to obtain a K atom number density of $n \approx 6 \times 10^{13}\ \mathrm{cm}^{-3}$; a circularly polarized 1 W broadband diode laser ('pump' laser) tuned to the centre of the D1 line at 770 nm; a linearly polarized 100 mW single frequency laser ('probe' laser) detuned by 1 nm from the D1 resonance; a Faraday rotator modulating the plane of polarization of the probe laser with an amplitude $\alpha \approx 0.02$ rad at a frequency $f_{\mathrm{mod}} = 2.9$ kHz; beam-shaping optics that produce a collimated probe beam with a cross-section of 4 mm × 19 mm; a polarization analyser, orthogonal to the polarizer; a seven-element photodiode array (shown in the top inset), with element separation of 0.31 cm along the $\hat{y}$-direction; and a 16-bit data acquisition system using a digital seven-channel lock-in amplifier to demodulate the signal proportional to the magnetic field B_y. Bottom inset, cross-section of the T-shaped cell, showing the rotation of the K polarization **P** into the $\hat{x}$ direction by an applied magnetic field B_y.

$$\delta B = \frac{1}{\gamma\sqrt{nT_2Vt}} \qquad \gamma = g\mu_B/\hbar(2I+1)$$

"A subfemtotesla multichannel atomic magnetometer,"
I. K. Kominis, T. W. Kornack, J. C. Allred & M. V. Romalis, Nature, Vol. 422, pp. 596-599 (2003).

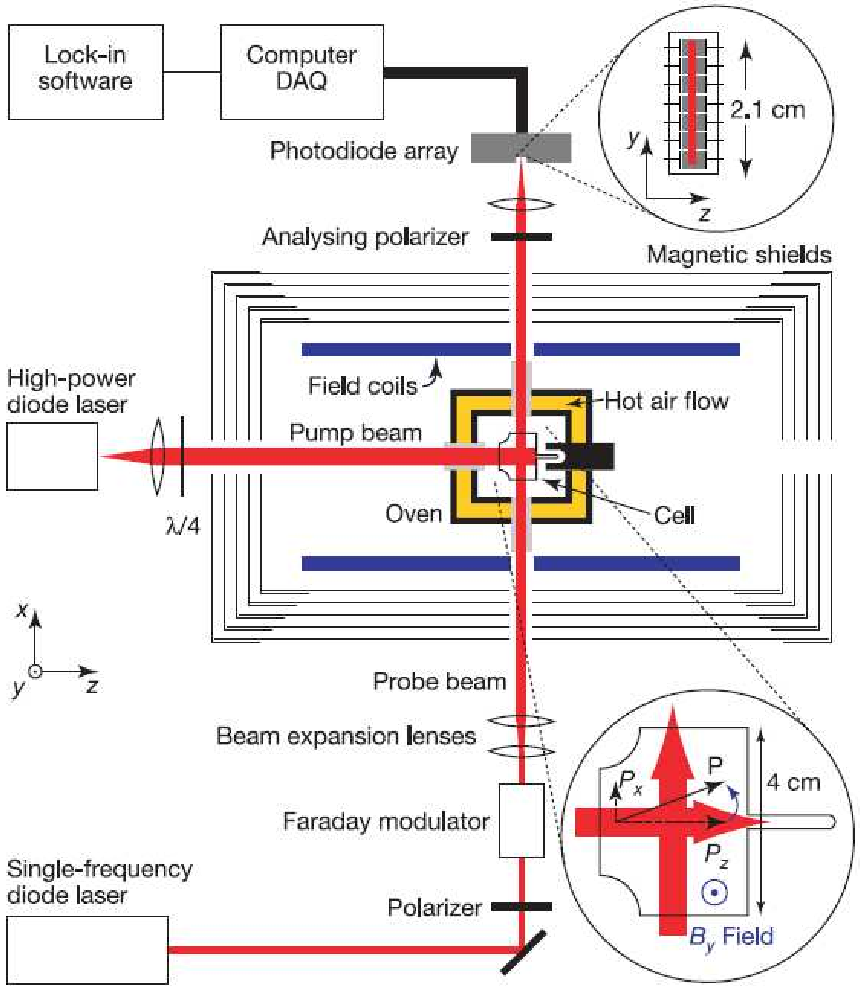

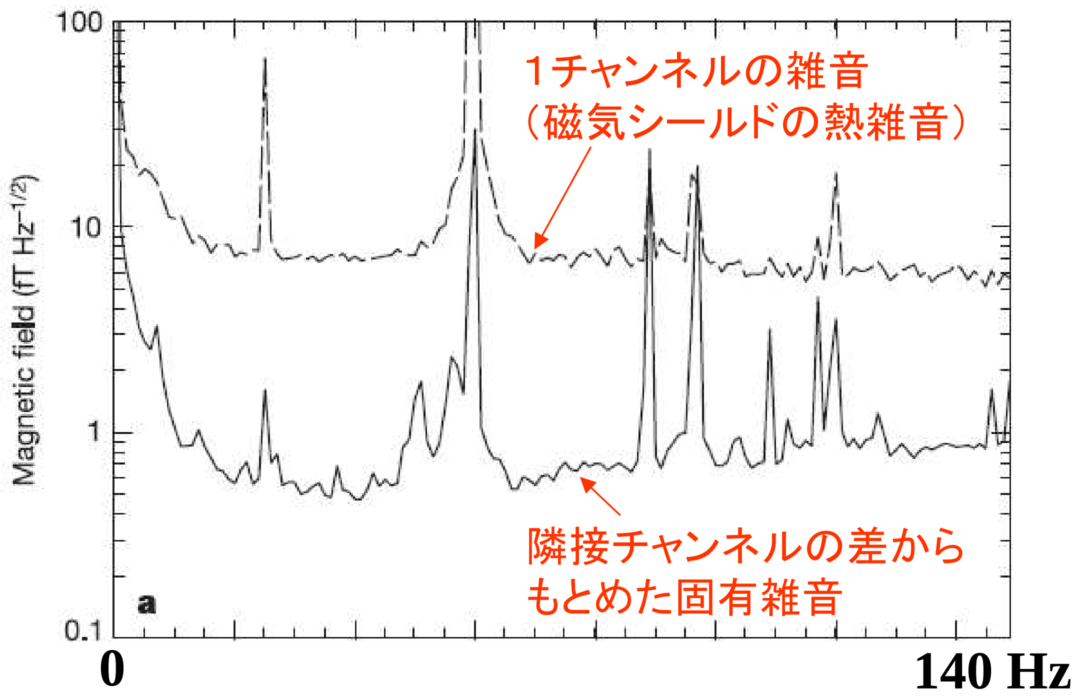

Figure 3 Magnetic field sensitivity and bandwidth of the magnetometer. Magnetic field noise in a single channel (**a**, dashed line), and intrinsic magnetic field sensitivity of a single channel extracted from the difference between adjacent channels (**a**, solid line). The magnetic field sensitivity data are obtained by recording the response of the magnetometer for about 100 s, performing a fast Fourier transform (FFT) without windowing; and calculating r.m.s. amplitudes in 1 Hz bins. A peak due to the calibrating B_y field is seen at 25 Hz. To obtain absolute field sensitivity, we divide the magnetometer FFT by a normalized frequency-response function shown in **b** with a fit to $A/(f^2 + B^2)^{1/2}$,

"High-Resolution Magnetometry with a Spinor Bose-Einstein Condensate,"

M. Vengalattore, J. M. Higbie, S. R. Leslie, J. Guzman, L. E. Sadler, and D. M. Stamper-Kurn, Phys. Rev. Lett., Vol. 98, 200801 (2007).

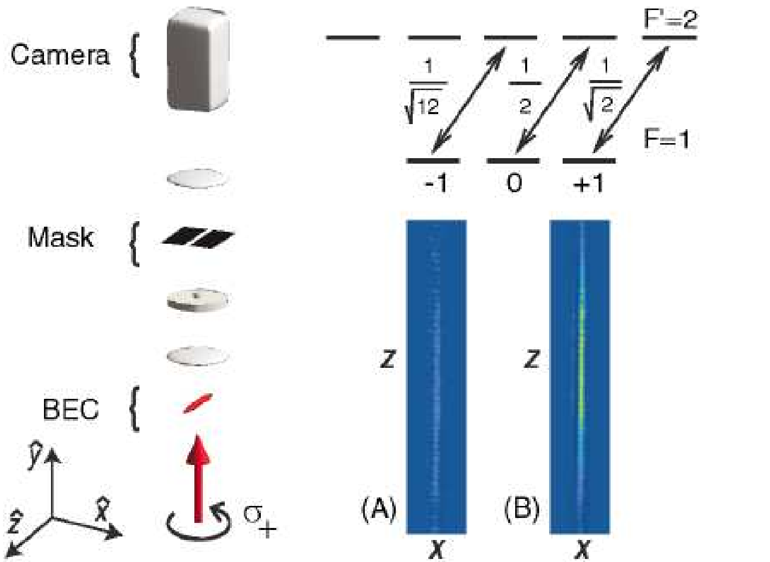

FIG. 1 (color). Imaging system for direct detection of atomic magnetization. Left: Circularly polarized probe light illuminates the trapped gas. A first lens and phase plate form a primary phase-contrast image which is selectively masked and then reimaged by a second lens onto the camera as one of ~40 frames which form a single composite image. Top right: Clebsch-Gordan coefficients for the imaging transition. Bottom right: Sample images of a BEC (a) with the atomic spin along $-\hat{y}$ and (b) with the spin along $+\hat{y}$, demonstrating the magnetization sensitivity of our technique.

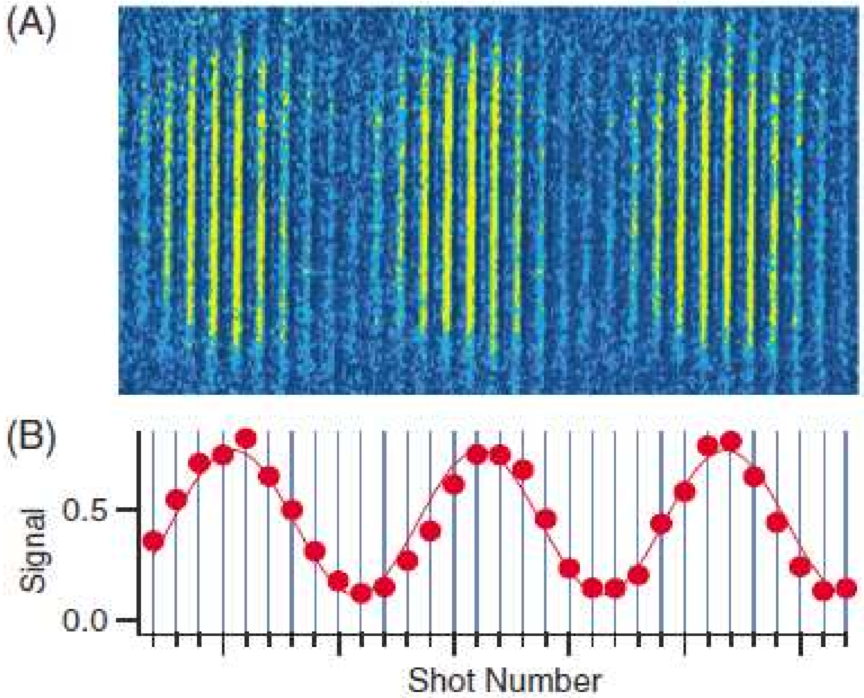

FIG. 2 (color). Direct imaging of Larmor precession of a spinor BEC through magnetization-sensitive phase-contrast imaging. Shown are 31 consecutive images each with 325 × 18 μm field of view. (a) Larmor precession is observed as a periodic modulation in the intensities of repeated images of a single condensate. (b) The peak signal strength oscillates at a rate which results from aliased sampling of a precisely measured 38.097(15) kHz Larmor precession at a sampling rate of 20 kHz.

Direct Nondestructive Imaging of Magnetization in a Spin-1 Bose-Einstein Gas,
J. M. Higbie, L. E. Sadler, S. Inouye, A. P. Chikkatur, S.R. Leslie, K. L. Moore, V. Savalli, and D. M. Stamper-Kurn,
PRL 95, 050401 (2005).

Atomic BEC with internal degrees of freedom

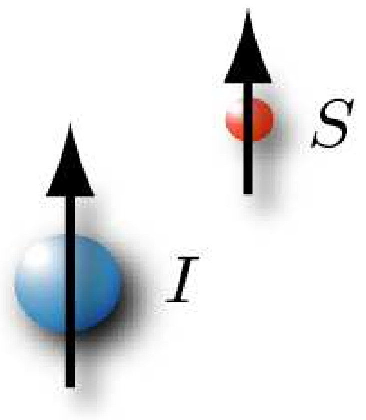

$$\boldsymbol{F} = \boldsymbol{S} + \boldsymbol{L} + \boldsymbol{I}$$

$\boldsymbol{S}$: electron spin

$\boldsymbol{L}$: electron orbital

$\boldsymbol{I}$: nuclear spin

^{87}Rb, ^{23}Na, ^{7}Li, ^{41}K	F =1, 2
^{85}Rb	F =2, 3
^{133}Cs	F =3, 4
^{52}Cr	F =3 (S =3, I =0)
^{4}He*, ^{40}Ca, ^{174}Yb, ^{176}Yb	F =0 (S =0, I =0)

unstable

^{87}Rb	high-field seeker		m_F	low-field seeker	
F=2	-2	-1	0	+1	+2
F=1		+1	0	-1	

スピン2ボース・アインシュタイン凝縮体におけるラーモア歳差運動の観測

磁力計実験方法

RF電磁波を用いてスピンを回す

RF電磁波を用いてスピンを回す

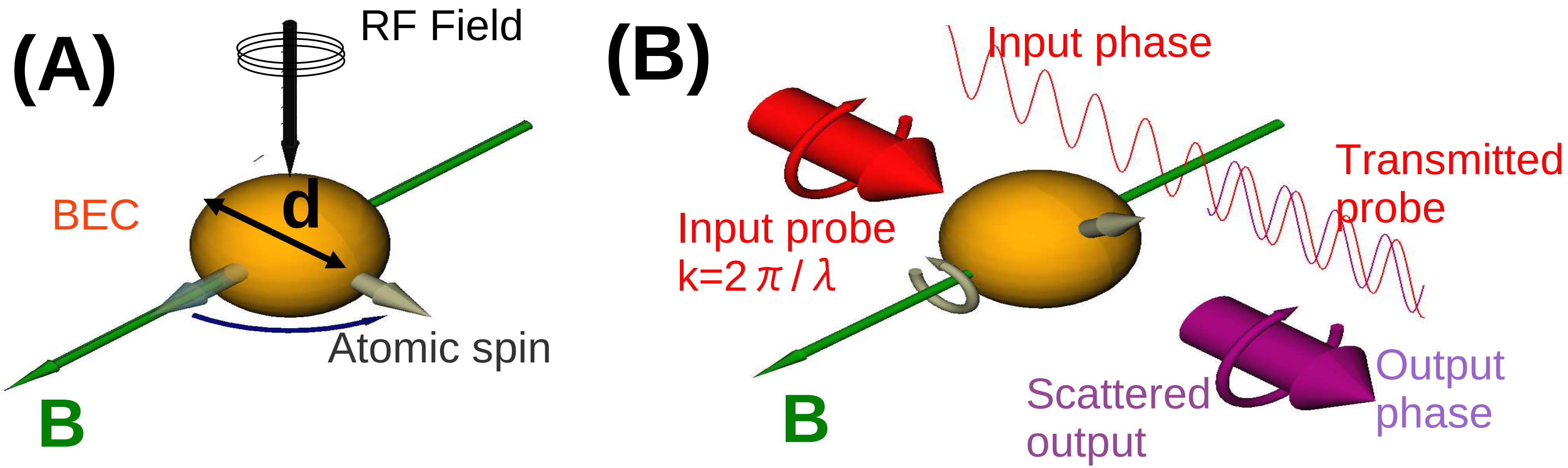

$$\phi_+ = kd(1 - n_+), \quad \phi_- = kd(1 - n_-)$$

Spinor^{87}Rbのボース凝縮体の生成

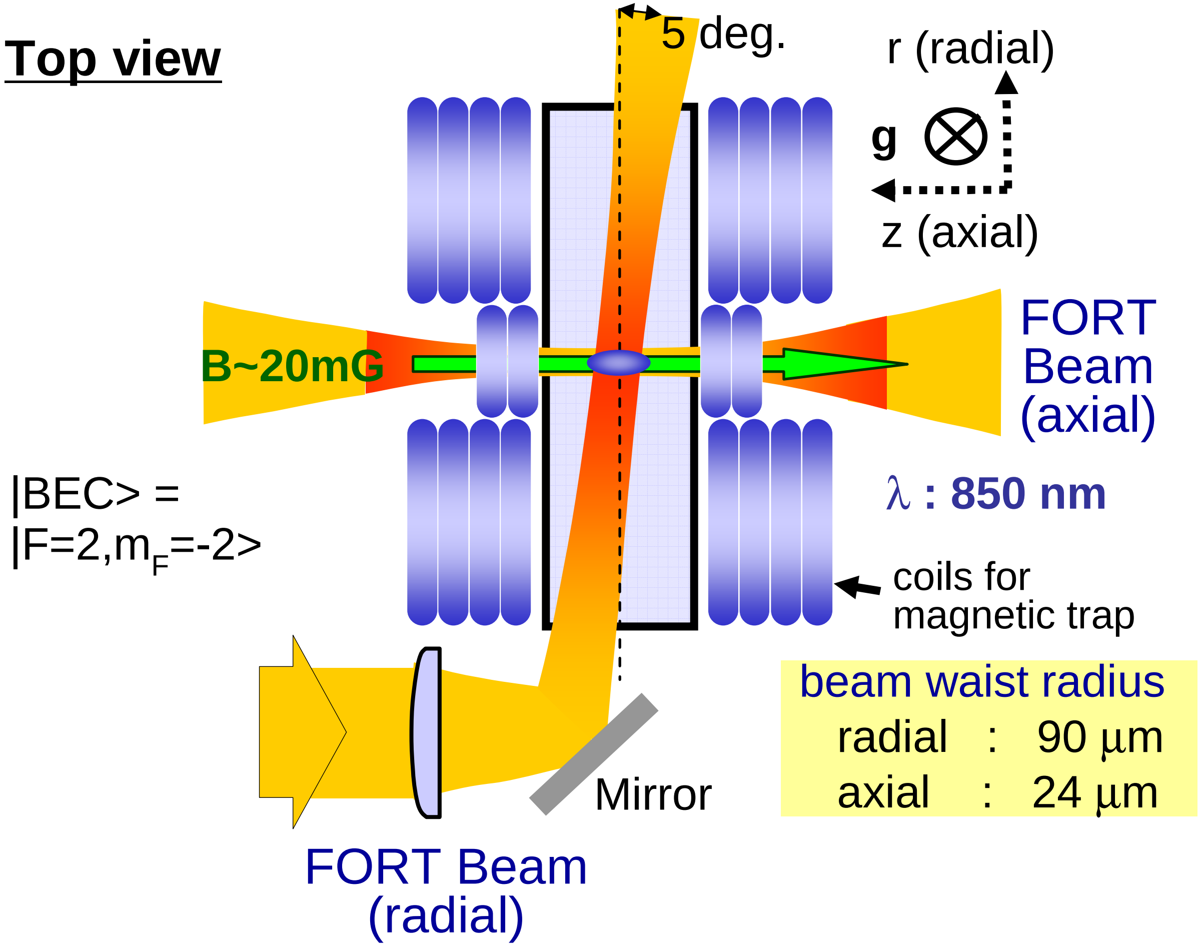

beam waist radius
radial : 90 μm
axial : 24 μm

potential depth of crossed FORT
U ~ 1.0 μK

位相差法と連続撮影

$$\frac{I_{\mathrm{atoms}}}{I_{\mathrm{no\ atoms}}} \approx 1 + 2\phi$$

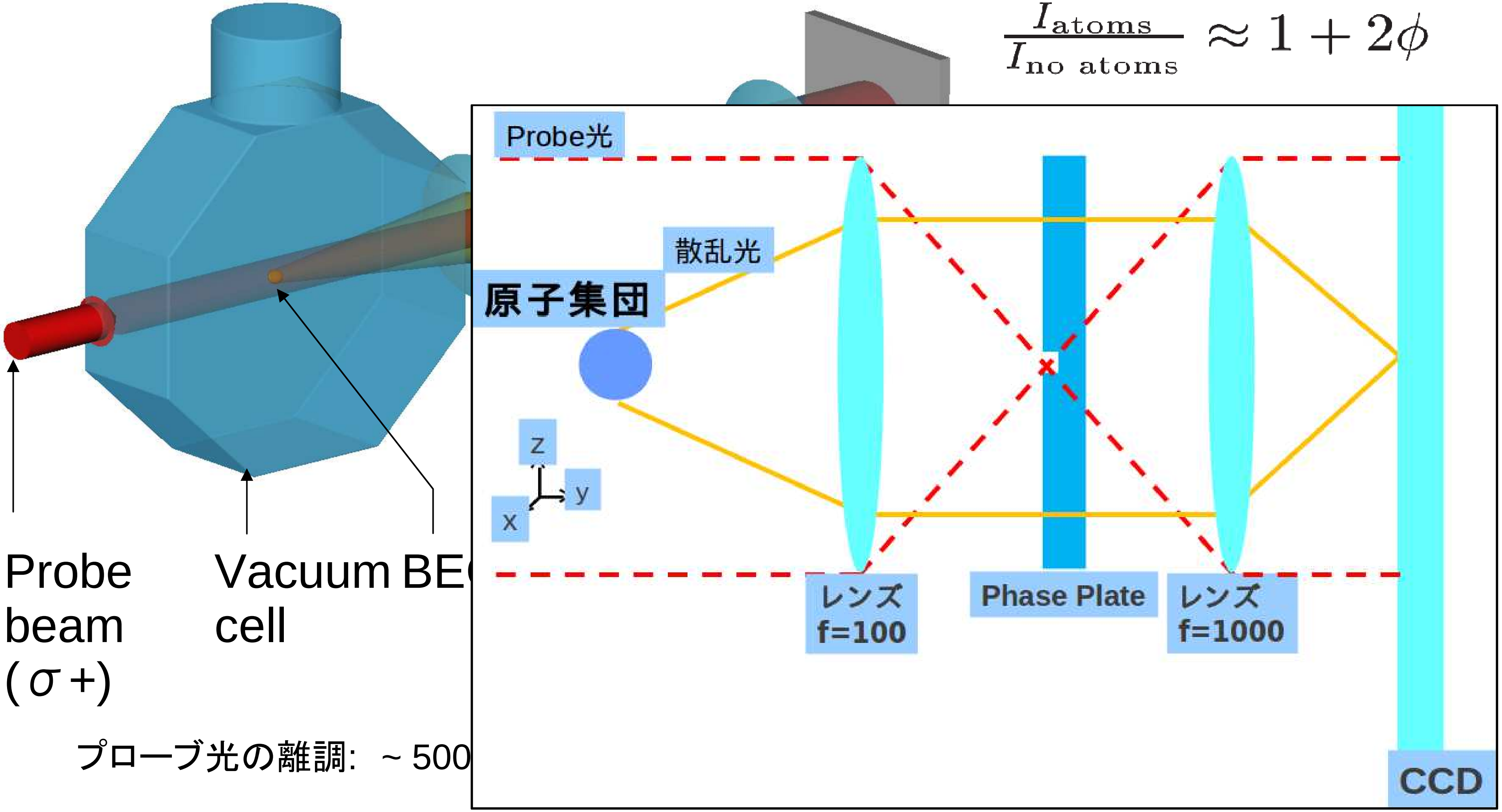

プローブ光の離調: ~500

位相差法と連続撮影

$$\frac{I_{\mathrm{atoms}}}{I_{\mathrm{no\ atoms}}} \approx 1 + 2\phi$$

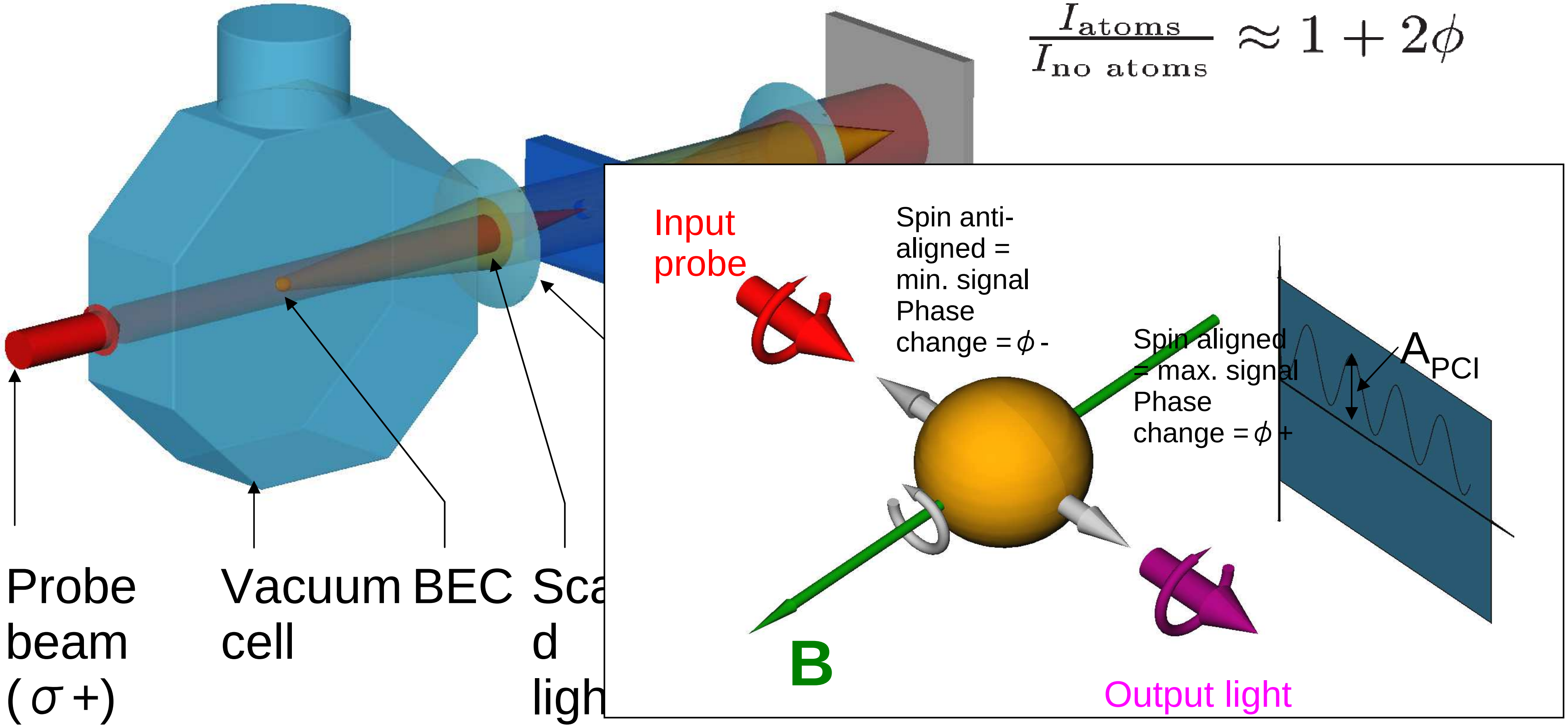

プローブ光の離調: ~ 500MHz, プローブ光強度: 1mW

位相差法と連続撮影

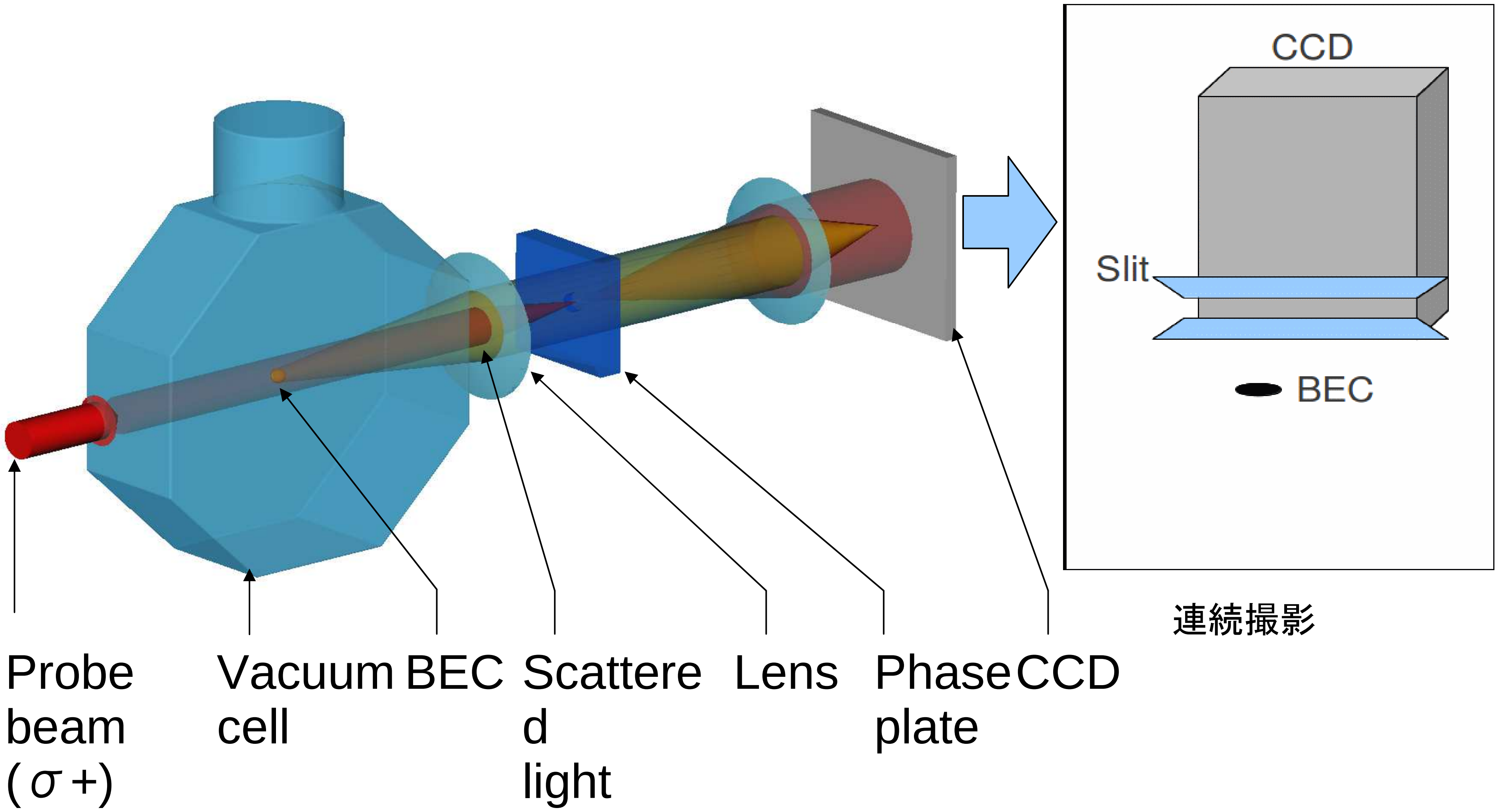

プローブ光の離調: ~ 500MHz, プローブ光強度: 1mW

Spatially resolved magnetometer

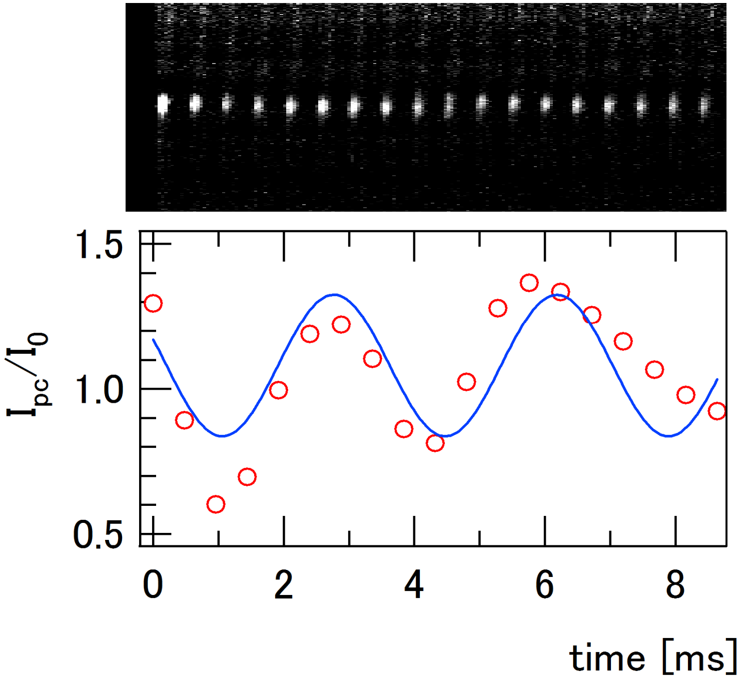

- 歳差運動を観測
- 磁場勾配のために歳差運動の周波数が原子の位置に依存
  → 位相のずれ

空間的依存性の解析方法

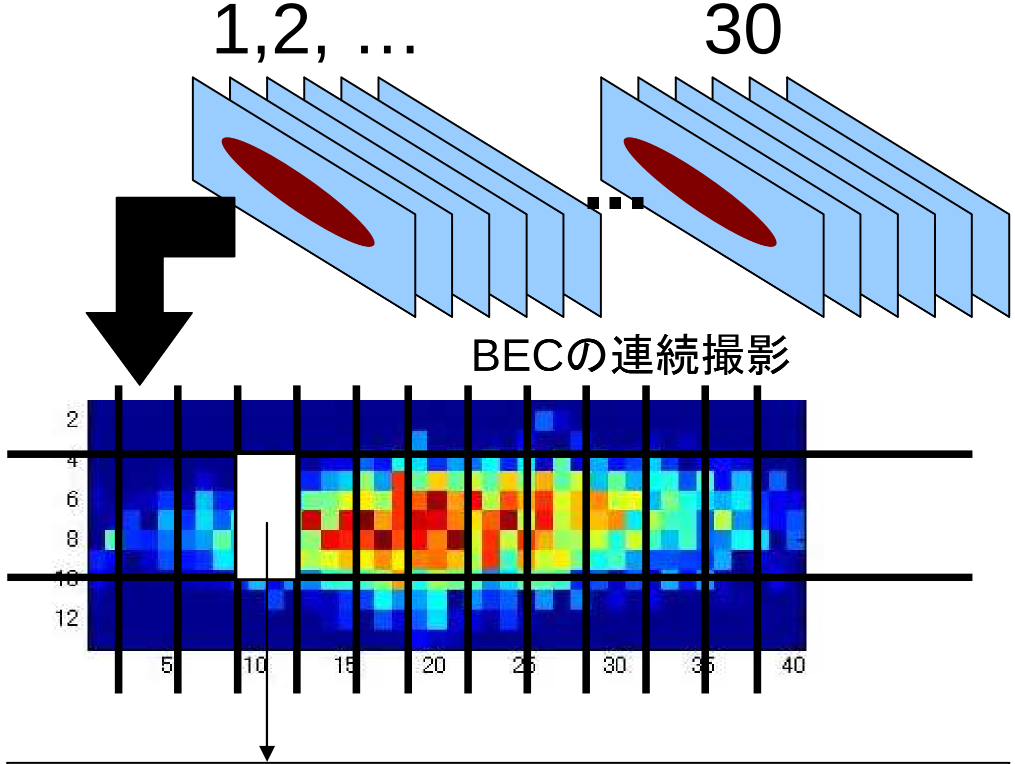

場所ごとのコントラストから、その場所の歳差運動周波数と位相を求める

NV中心を使った磁力計 1

nature Vol 455 | 2 October 2008 | doi:10.1038/nature07279

LETTERS

Nanoscale magnetic sensing with an individual electronic spin in diamond

J. R. Maze[1], P. L. Stanwix[2], J. S. Hodges[1,3], S. Hong[1], J. M. Taylor[4], P. Cappellaro[1,2], L. Jiang[1], M. V. Gurudev Dutt[5], E. Togan[1], A. S. Zibrov[1], A. Yacoby[1], R. L. Walsworth[1,2] & M. D. Lukin[1]

１個の電子から10nm離れた場所の磁場 ～ 1μT

→ ナノメートルの空間分解とマイクロテスラの感度の磁力計の重要性

・30nmの直径のダイヤモンドのナノクリスタルを用いて 0.5μT $Hz^{-1/2}$ を実現

・デコヒーレンス制御と量子ビット読み出し技術を利用

NV中心を使った磁力計 2

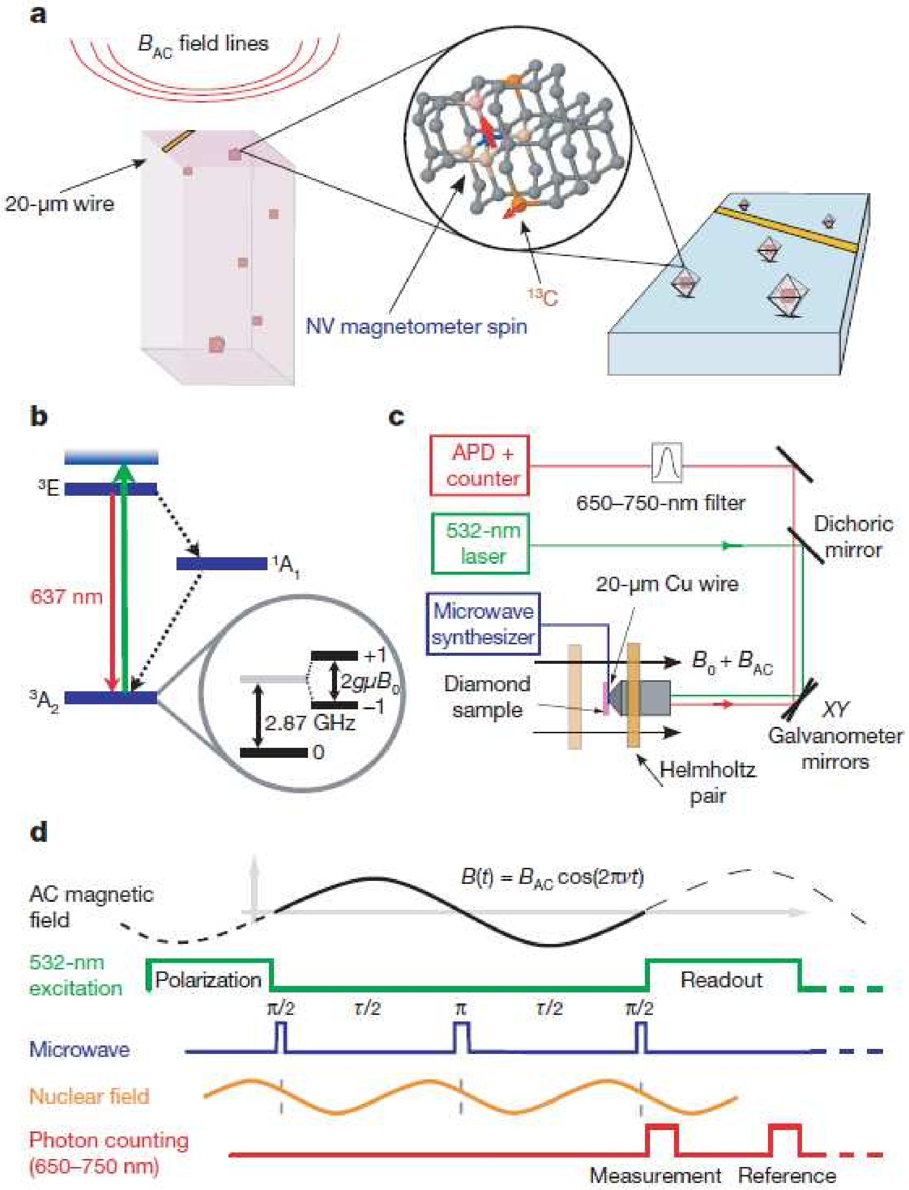

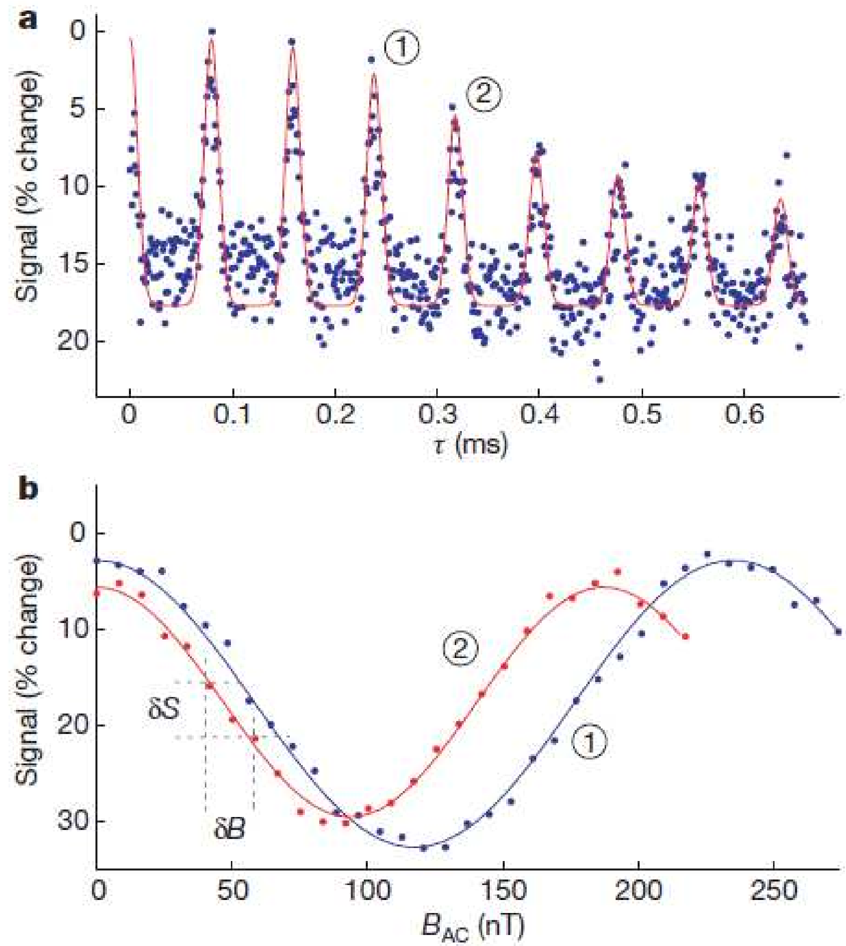

NV中心を使った磁力計 3

Magnetic field imaging with nitrogen-vacancy ensembles

New Journal of Physics **13** (2011) 045021

L M Pham[1], D Le Sage[2], P L Stanwix[2], T K Yeung[1,3], D Glenn[2],
A Trifonov[3,4], P Cappellaro[5], P R Hemmer[6], M D Lukin[3],
H Park[3,7], A Yacoby[3] and R L Walsworth[2,3,8]

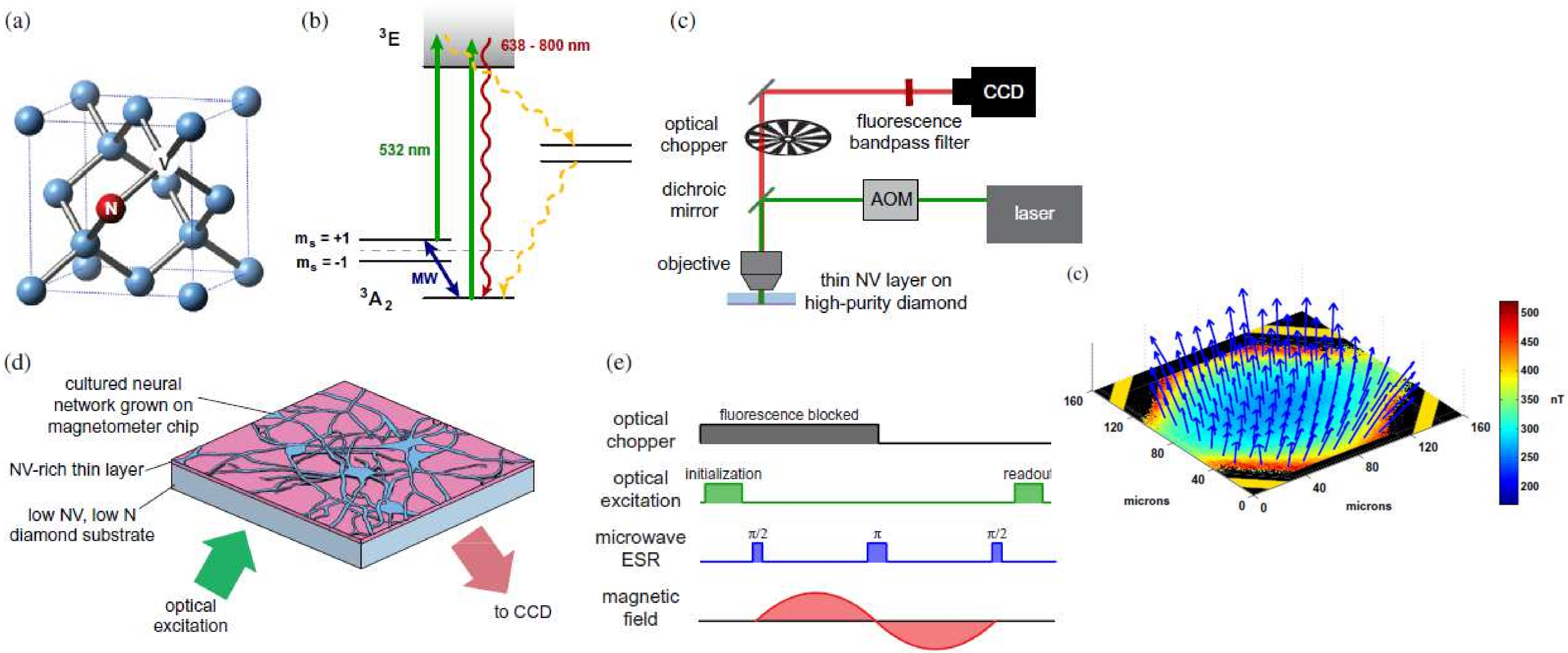

Outline

1. Introduction

2. Magnetometer

3. Quantum enhanced measurements

4. Scaling

5. Conclusions

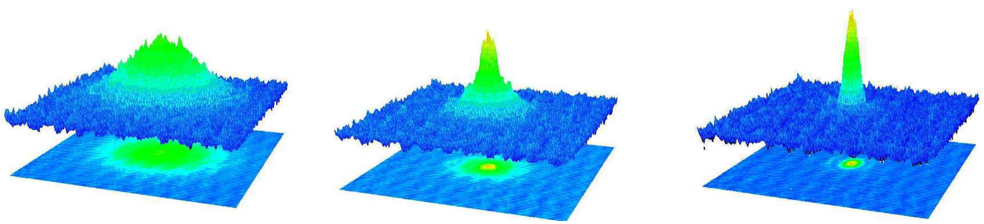

Quantum-enhanced gravitational-wave detector

"Quantum-mechanical noise in an interferometer," Carlton M. Caves, Phys. Rev. D, 23, 1693 (1981).

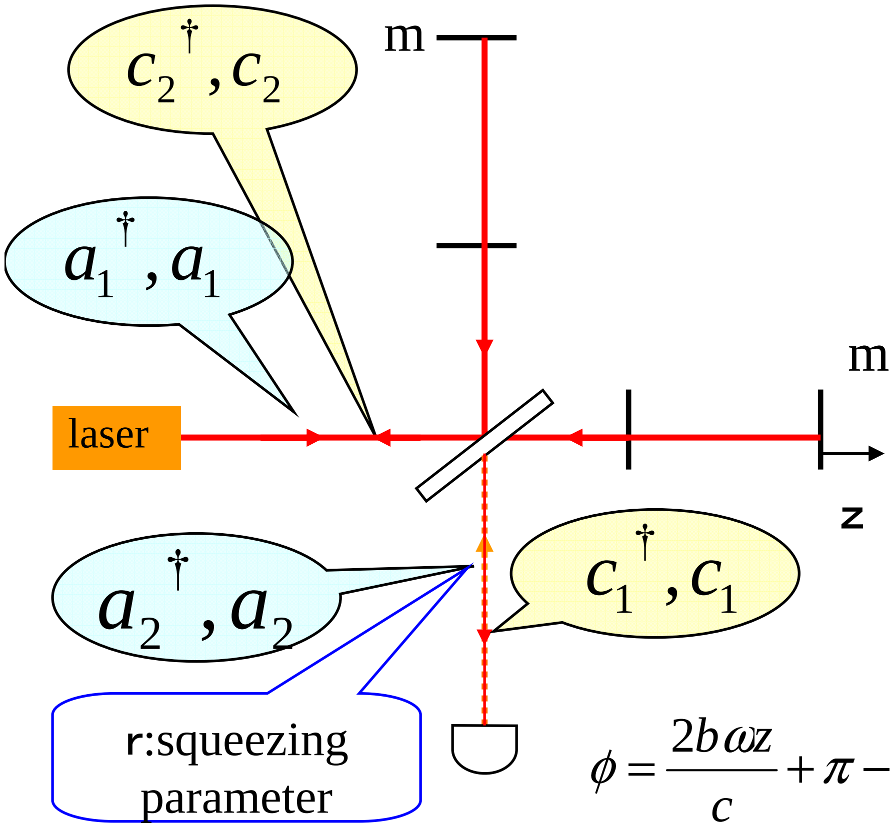

$$\phi = \frac{2b\omega z}{c} + \pi - 2\mu$$

μ : relative phase

b : number of bounce	c : light velocity
τ : observation time	ω : frequency
α : laser power	$\hbar$: planck's constant

Photon counting error

$$n_{out} \equiv c_1^\dagger c_1 \qquad z \to z + \delta z$$

$$\delta n_{out} \cong \alpha^2 \left(\frac{2b\omega}{c}\right) \sin\left(\frac{\phi}{2}\right) \cos\left(\frac{\phi}{2}\right) \delta z \qquad \frac{\Delta z}{\delta z} = \frac{\Delta n_{out}}{\delta n_{out}}$$

$$\boxed{(\Delta z)_{pc} \cong \left(\frac{c}{2b\omega}\right)\left(\frac{e^{-2r}}{\alpha^2} + \frac{\sinh^2 r}{\alpha^4}\right)^{\frac{1}{2}}}$$

Radiation pressure error

$$\wp \equiv \left(\frac{2b\hbar\omega}{c}\right)(b_2^\dagger b_2 - b_1^\dagger b_1)$$

$$(\Delta\wp)^2 = \left(\frac{2b\hbar\omega}{c}\right)^2 (\alpha^2 e^{2r} + \sinh^2 r)$$

$$(\Delta z)_{rp} \cong \frac{(\Delta\wp)\tau}{2m}$$

$$= \left(\frac{b\hbar\omega\tau}{mc}\right)(\alpha^2 e^{2r} + \sinh^2 r)^{\frac{1}{2}}$$

Quantum-enhanced gravitational-wave detector

"Quantum-mechanical noise in an interferometer," Carlton M. Caves, Phys. Rev. D, 23, 1693 (1981).

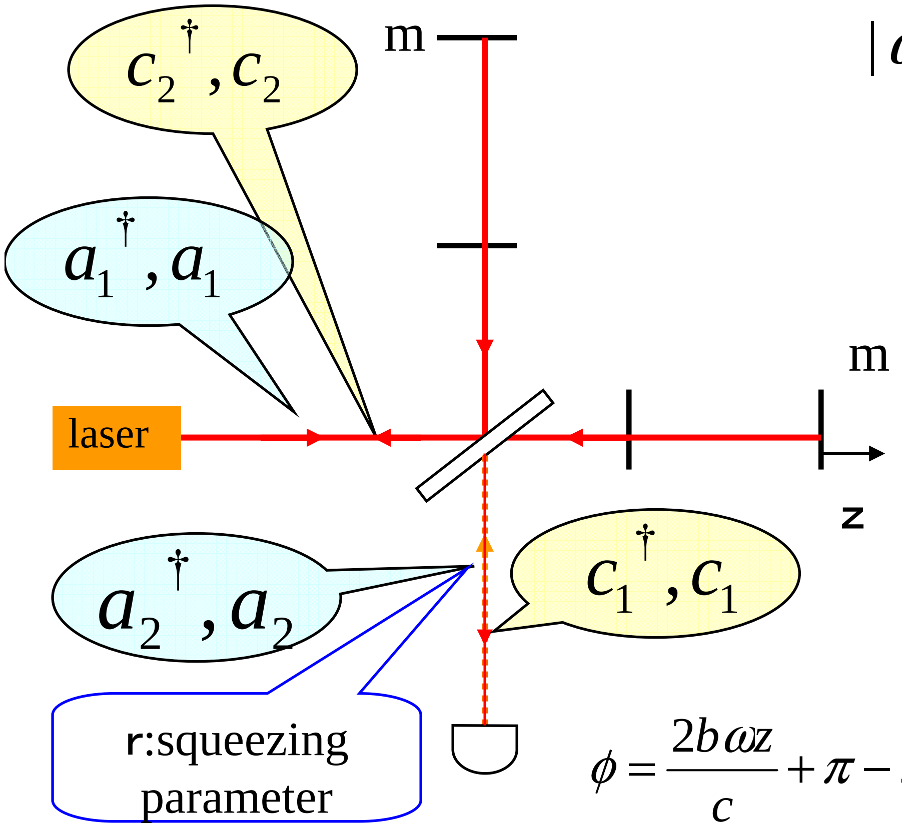

$$\phi = \frac{2b\omega z}{c} + \pi - 2\mu$$

μ : relative phase

$$|\alpha| \gg \sinh^2 r$$

$$(\Delta z)_{rp} \sim \left(\frac{b\hbar\omega\tau}{mc}\right)|\alpha| e^{r} \qquad (\Delta z)_{pc} \sim \left(\frac{c}{2b\omega}\right)\frac{e^{-r}}{|\alpha|}$$

$$\Delta z = \{(\Delta z)_{pc}{}^2 + (\Delta z)_{rp}{}^2\}^{\frac{1}{2}}$$

$$\text{Minimum when} (\Delta z)_{pc} = (\Delta z)_{rp}$$

$$|\alpha|^2 = \frac{1}{2}\left(\frac{mc^2}{\hbar\omega}\right)\left(\frac{1}{\omega\tau}\right)\left(\frac{1}{b^2}\right)e^{-2r} = \alpha_{opt}{}^2$$

$$\Delta z_{opt} = \left(\frac{\hbar\tau}{m}\right)^{\frac{1}{2}} \cong (\Delta z)_{SQL}$$

b : number of bounce	c : light velocity
τ : observation time	ω : frequency
α : laser power	$\hbar$: planck's constant

“A gravitational wave observatory operating beyond the quantum shot-noise limit," The LIGO Scientific Collaboration, Nature Physics, Vol. 7, 962 (2011).

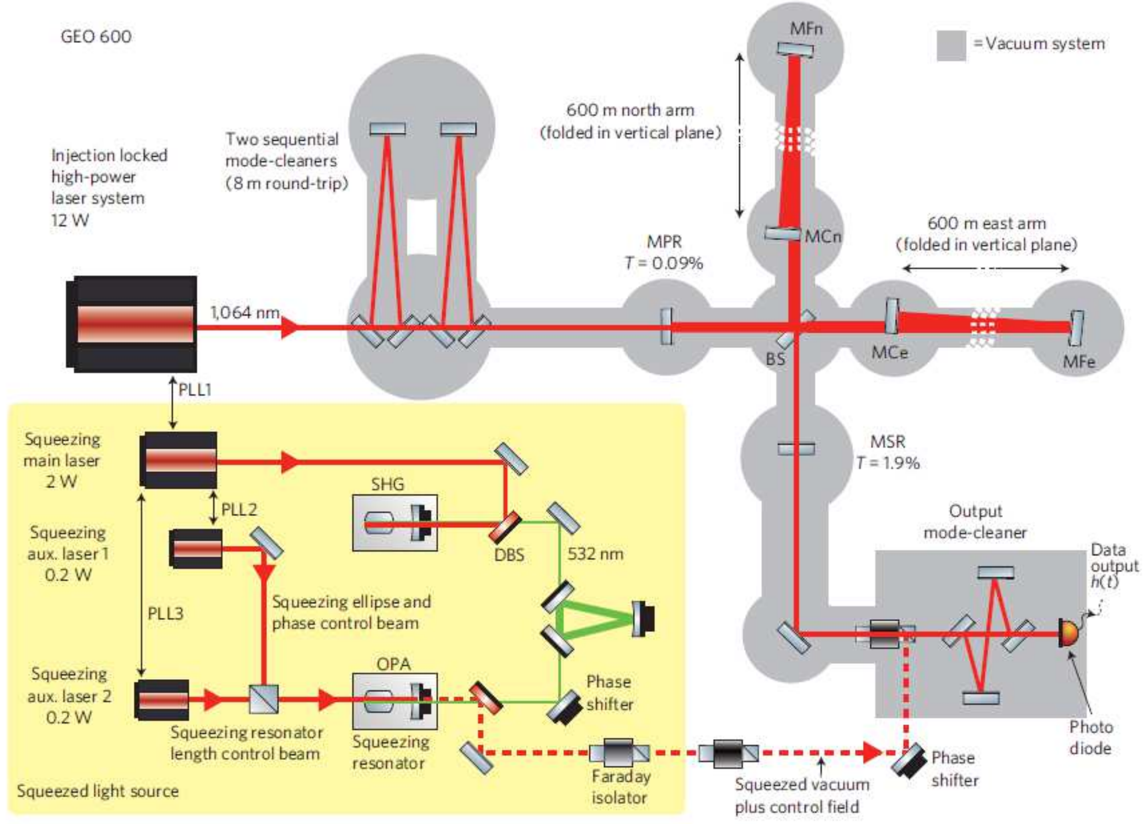

Figure 1 | Simplified optical layout of the squeezed-light enhanced GEO 600 observatory. The observatory consists of the conventional GEO 600 and the additional squeezed-light source (yellow box, see Methods summary for details). The observatory has two singly folded arms with a total optical length of 2,400 m. A GW passing from most directions will shorten one arm, while the length of the perpendicularly orientated arm is increased, and vice versa in the next half-cycle of a passing wave, producing a periodic power change of the output light that is detected by a photo diode. The observatory is operated such that almost all the light is back-reflected towards the 12 W input laser system, by keeping the interferometer output on a dark fringe by means of a control system. A power-recycling mirror (MPR) leads to a resonant enhancement of the circulating light power of 2.7 kW at the beamsplitter. Similar to the power-recycling technique, a partially transmissive signal-recycling mirror (MSR) is installed to further resonantly enhance the GW-induced signal at the interferometer's output. BS: 50/50 beamsplitter, SHG: second harmonic generator, OPA: optical parametric amplifier, DBS: dichroic beamsplitter, PLL: phase locking loop, MFe/MFn: far interferometer end mirrors (east/north), MCe/MCn : central interferometer mirrors, T: mirror transmissivity. All interferometer optics are suspended by multi-stage pendulums and situated in a vacuum system.

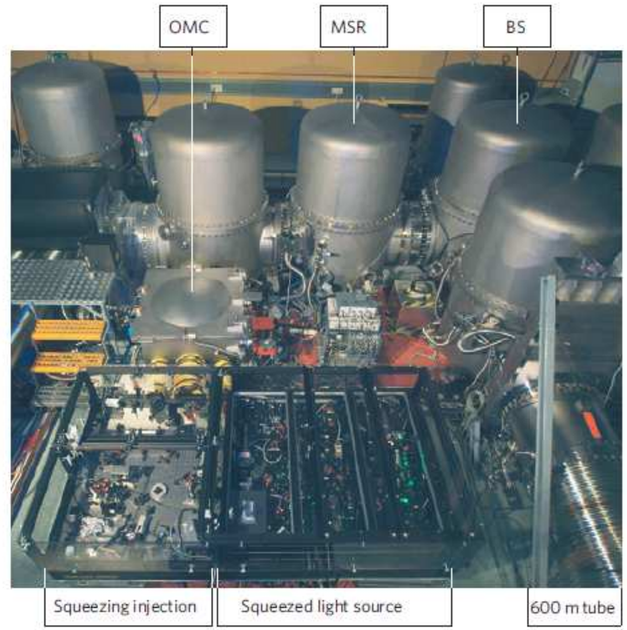

Figure 2 | View into the GEO 600 central building. In the front, the squeezing bench containing the squeezed-light source and the squeezing injection path is shown. The optical table is surrounded by several vacuum chambers containing suspended interferometer optics.

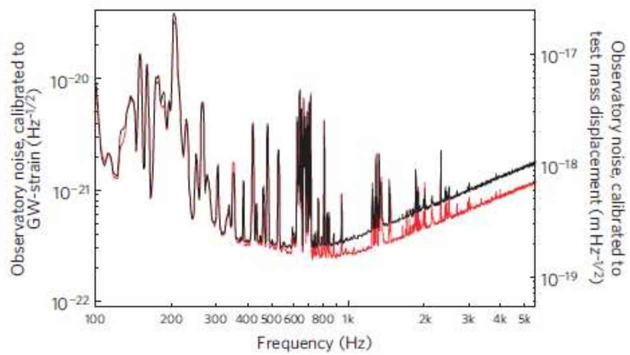

3rd generation gravitational wave detector   http://www.et-gw.eu/

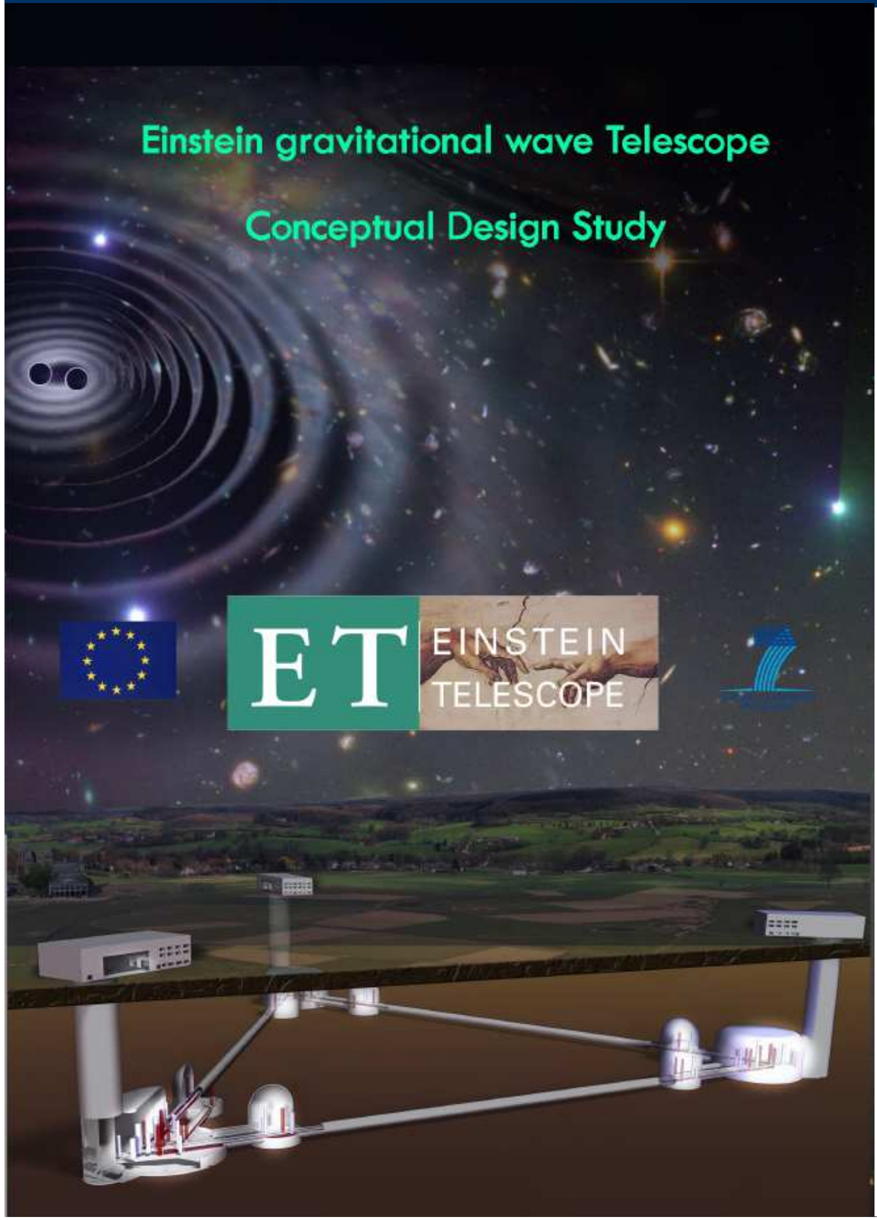

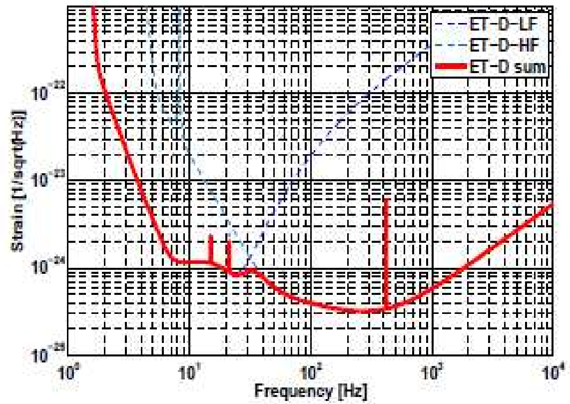

Figure 7: Sensitivity of the Einstein Telescope in the 'xylophone' configuration. The sensitivity of the low-frequency cryogenic interferometer is shown in the dashed dark blue curve and the one of the high-frequency room temperature one in a dashed blue-green tone. The sum of both is given by the solid bright red curve.

A summary of all the optical parameters of the Einstein Telescope baseline design is given in the table below:

	ET-HF	ET-LF
Approximate frequency range	10–10^4 Hz	1–250 Hz
Detection scheme	DC readout	DC readout
Input power (after IMC)	500 W	3 W
Laser wavelength	1064 nm	1550 nm
Beam shape	LG_{33}	TEM_{00}
ARM CAVITIES		
Arm length	10 km	10 km
Opening angle	60°	60°
Arm power	3 MW	18 kW
Temperature	290 K	10 K
Mirror material	fused silica	silicon
Mirror diameter	62 cm	>45 cm
Mirror thickness	30 cm	about 50 cm
Mirror mass	200 kg	211 kg
Beam radius (at mirror)	7.2 cm	9.0 cm
Beam waist (symmetric cavity)	2.51 cm	2.9 cm
RoC (symmetric cavity)	5690 m	5580 m
Scatter loss per surface	37.5 ppm	37.5 ppm
Finesse	880	880
Reflective coating ITM	tantala/silica 8 $\lambda/4$ doublets	tantala/silica 9 $\lambda/4$ doublets
Reflective coating ETM	tantala/silica 17 $\lambda/4$ doublets	tantala/silica 18 $\lambda/4$ doublets
Transmission ITM	7000 ppm	7000 ppm
Transmission ETM	6 ppm	6 ppm

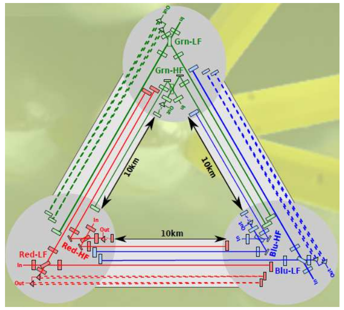

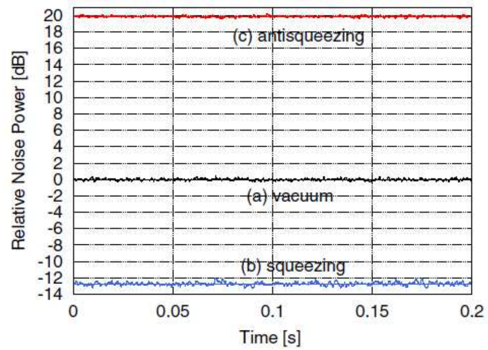

12.7 dB @ 1064 nm
PRL 104, 251102 (2010)

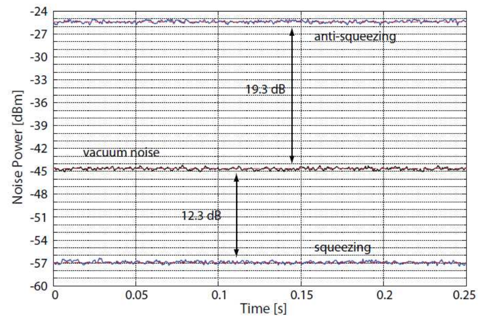

12.3 dB @ 1550 nm
Opt.Express, 19, 25763 (2011)

Quantum magnetometer

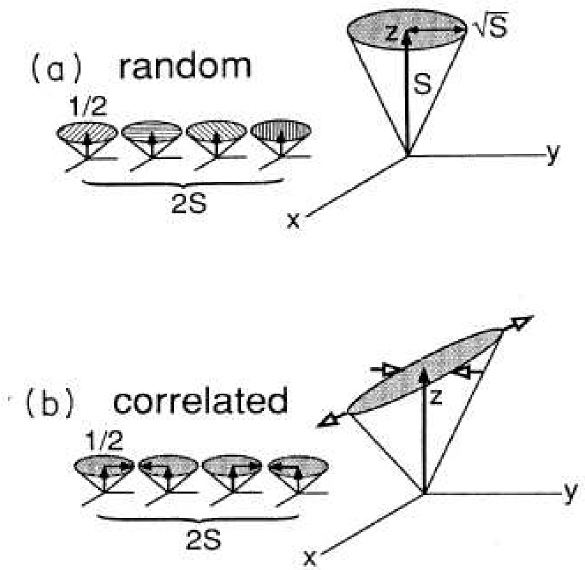

"Squeezed spin states," Masahiro Kitagawa and Masahito Ueda, Phys. Rev. A 47, 5138–5143 (1993)

Angular momentum system

$$\vec{S} = (S_x, S_y, S_z) \qquad S_i = \sum_{n=1}^{N} \sigma_i^{(n)} / 2$$

Cyclic commutation relation

$$[S_i, S_j] = i\varepsilon_{ijk} S_k$$

$$\Rightarrow (\Delta S_i^2)(\Delta S_j^2) \geq \frac{1}{4} \left| \langle S_k \rangle \right|^2$$

For *N* atoms in m_F=*F* along the quantization axis z,

$$S_z = FN$$

A magnetic field along *y* axis causes a rotation of *S* in *x*-*z* plane. Polarization of light propagating along *x* will be rotated propotional to S_x. This measument is limited by the projection noise of the atom,

$$(\Delta S_x^2) = \frac{S_z}{2} = FN/2$$

and light shot noise of polarization measurement.

"Sub-Projection-Noise Sensitivity in Broadband Atomic Magnetometry,"

M. Koschorreck, M. Napolitano, B. Dubost, and M. W. Mitchell, Phys. Rev. Lett., Vol. 104, 093602 (2010).

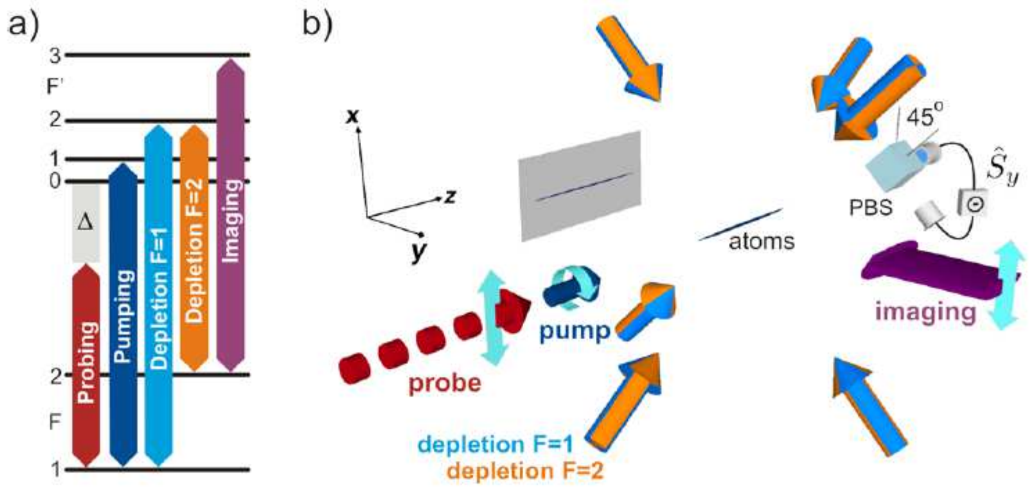

FIG. 1 (color online). (a) Atomic transitions for probing, preparation, and imaging light fields. (b) Atomic ensemble with probing, pumping, and imaging light fields. The polarimeter measures in the 45° basis, i.e., the Stokes component $\hat{S}_y$.

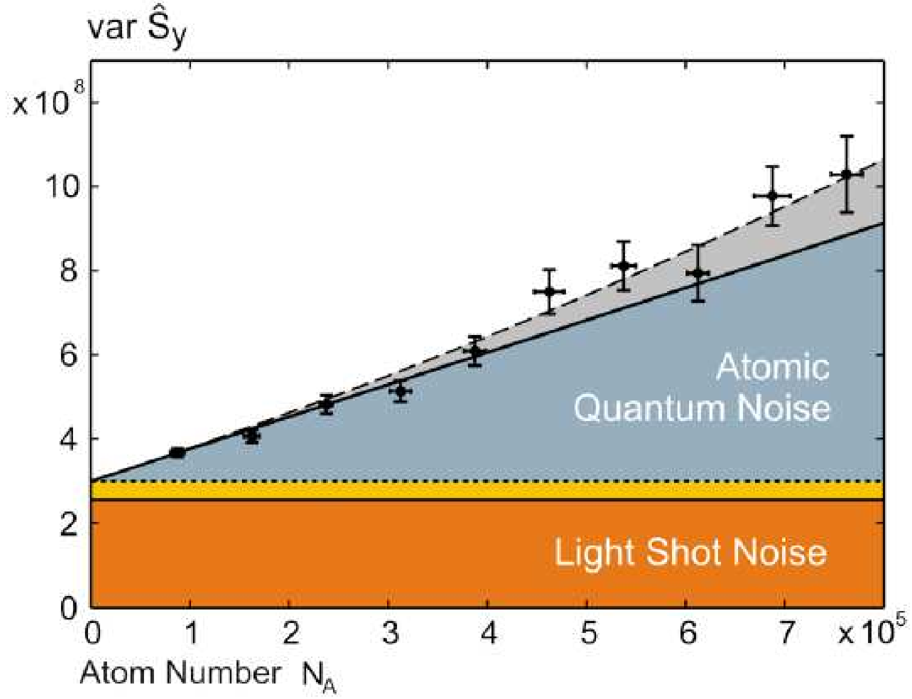

FIG. 3 (color online). Measured variance of $\hat{S}_y$ with statistical errors for $N_L = 10^9$ as a function of atom number. Dashed curve: theoretical curve including technical noise sources. Solid line: pure spin quantum noise. Dotted line: shot noise and technical light noise. Thin solid line: light shot noise. The electronic noise is not plotted because it is negligible for this number of photons.

Laser cooled Rb atoms, 10^6, 25μK, dipole trap
20 times QND measurement w/o dipole trap

"Spin Squeezing of a Cold Atomic Ensemble with the Nuclear Spin of One-Half",
T. Takano, M. Fuyama, R. Namiki, and Y. Takahashi, Phys. Rev. Lett. 102, 033601 (2009).

"Squeezed-Light Optical Magnetometry," Florian Wolfgramm, Alessandro Cerè, Federica A. Beduini, Ana Predojević, Marco Koschorreck, and Morgan W. Mitchell , Phys. Rev. Lett., Vol. 105, 053601 (2010).

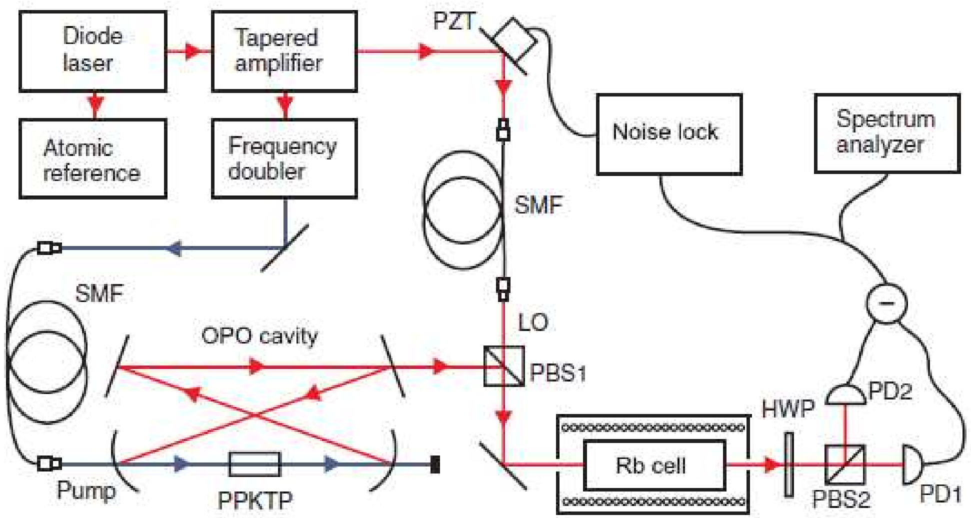

FIG. 1 (color online). Experimental apparatus. Rb cell, rubidium vapor cell with magnetic coil and magnetic shielding; OPO, optical parametric oscillator; PPKTP, phase-matched nonlinear crystal; LO, local oscillator beam; PBS, polarizing beam splitter; HWP, half-wave plate; SMF, single-mode fiber; PD, photodiode.

Hot Rb atoms, 794.7 nm, D1 line

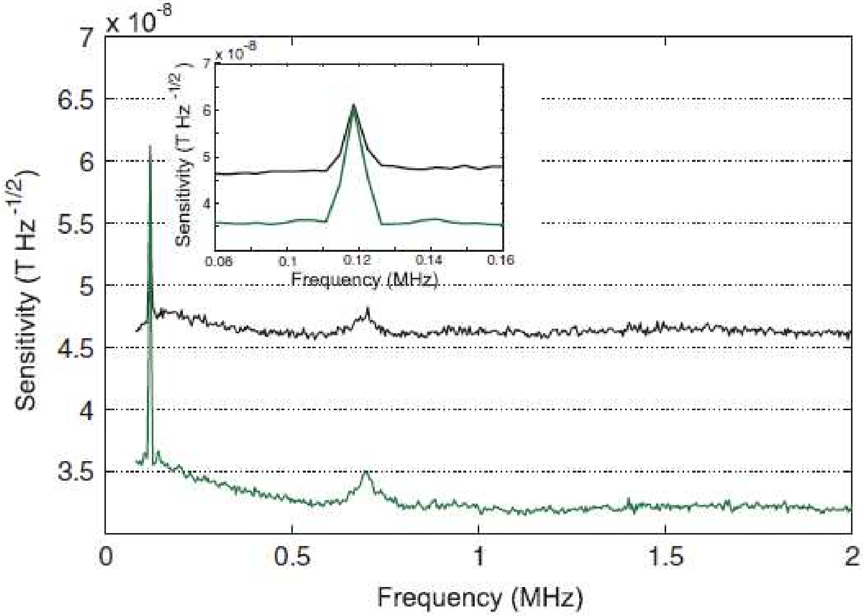

FIG. 3 (color online). Faraday rotation measurement. Power of the polarization signal as center frequency is scanned, $RBW = 3$ kHz, $VBW = 30$ Hz. The (upper) black curve shows the applied magnetic signal at 120 kHz above the shot-noise background of a polarized (but not squeezed) probe. The (lower) green line depicts the same signal with polarization-squeezing. A zoomed view around the calibration peak at 120 kHz is shown in the inset.

-3.2 dB, 3.2 x 10^{-8} T/√Hz

"Atom-chip-based generation of entanglement for quantum metrology,"

Max F. Riedel1, Pascal Böhi, Yun Li, Theodor W. Hänsch, Alice Sinatra & Philipp Treutlein, Nature, 464, 1170 (2010).

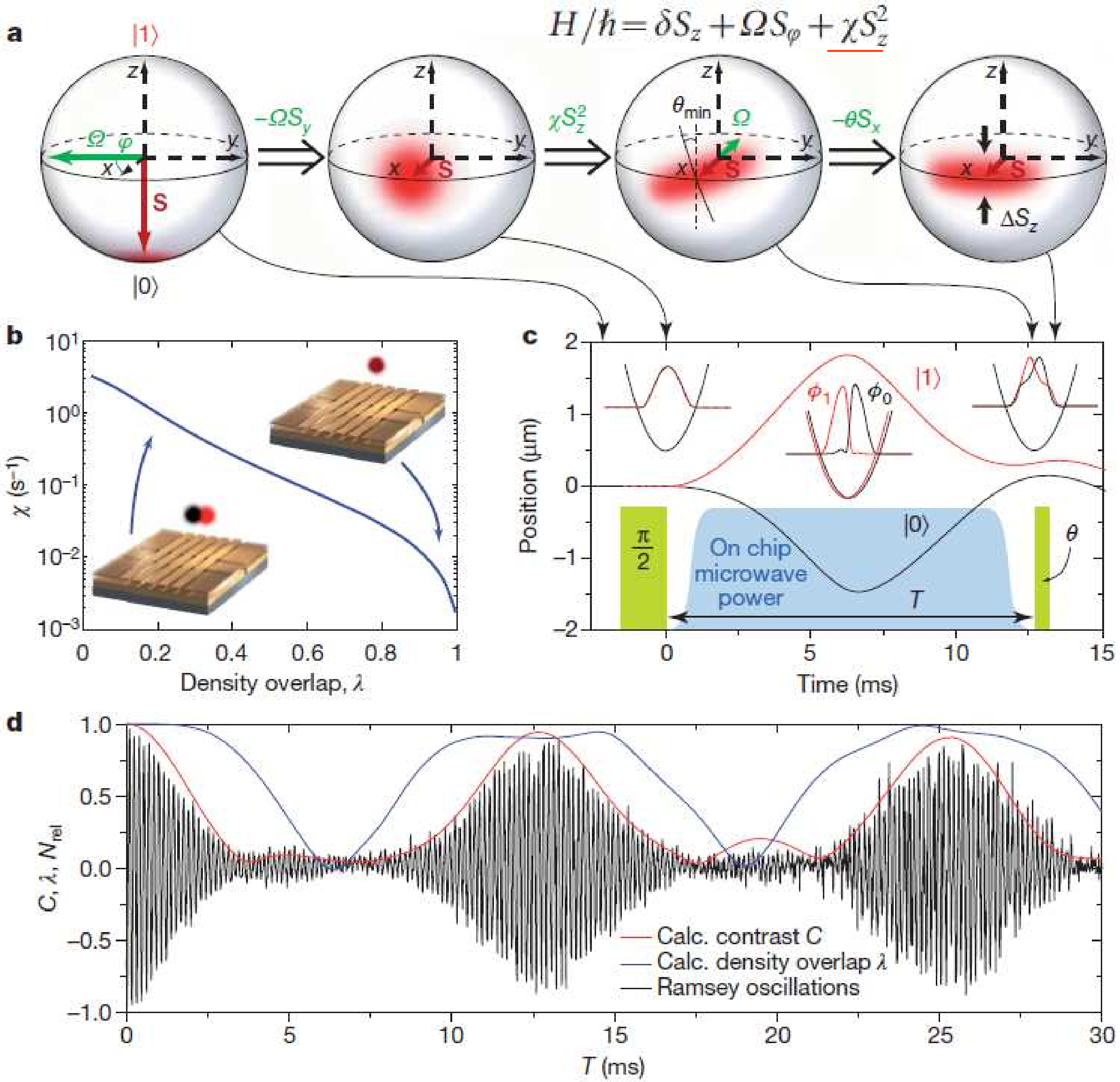

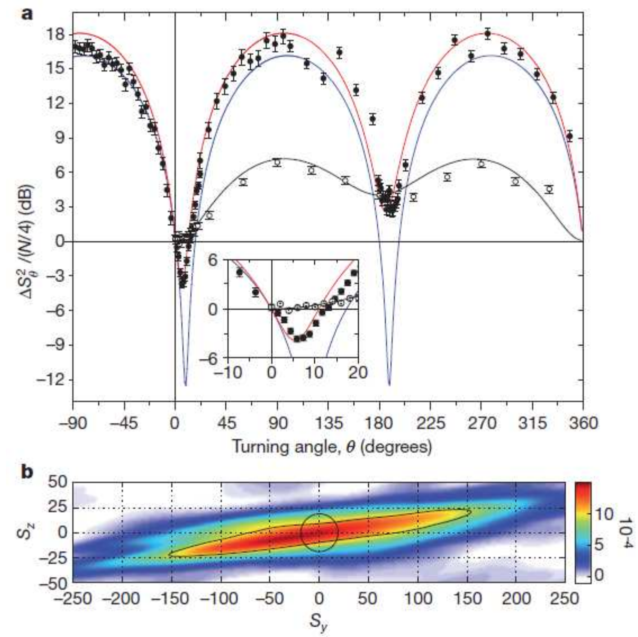

Figure 2 | Spin noise tomography and reconstructed Wigner function of the spin-squeezed BEC. **a**, Observed spin noise for the spin-squeezed state (filled circles) and for a coherent spin state (reference measurement, open circles). The normalized variance $\Delta_n S_\theta^2 = 4\Delta S_\theta^2/\langle N\rangle$ is shown as a function of the turning angle θ in the y–z plane, with error bars corresponding to ±s.d. For this graph, we remove photon shot noise due to the imaging process as described in the Supplementary Information. In the squeezed state, a spin-noise reduction of -3.7 ± 0.4 dB is observed for $\theta_{min} = 6°$, corresponding to $\xi^2 = -2.5 \pm 0.6$ dB of metrologically useful squeezing for our Ramsey contrast of $C = (88 \pm 3)$%. Solid lines are results from our dynamical simulation: blue, squeezed state with losses but without technical noise; red, squeezed state with losses and technical noise; black, reference measurement with losses and technical noise. Inset, zoom in for small angles. **b**, Wigner function of the spin-squeezed BEC reconstructed from our measurements. The black contour line indicates where the Wigner function has fallen to $1/\sqrt{e}$ of its maximum. Squeezed and 'anti-squeezed' quadratures are clearly visible. For comparison, the circular $1/\sqrt{e}$ contour of an ideal coherent spin state is shown. The area of the contour line is larger than the area of the circle, indicating that the squeezed state is no longer a minimum uncertainty state.

"Spin-nematic squeezed vacuum in a quantum gas,"
C. D. Hamley, C. S. Gerving, T. M. Hoang, E. M. Bookjans and M. S. Chapman, Nature Physics, 8, 305 (2012).

Spin-1 system → SU(3) → 3^2-1=8 components

$$\begin{cases} \hat{S}_i \\ \hat{Q}_{ij} = \hat{S}_i\hat{S}_j + \hat{S}_j\hat{S}_i - (4/3)\delta_{ij} \end{cases}$$

Quadrupole tensor is symmetric and traceless.

$[\downarrow,\rightarrow]$	S_y	S_z	Q_{yz}	Q_{xz}	Q_{xy}	Q_{xx}	Q_{yy}	Q_{zz}
S_x	iS_z	$-iS_y$	$i(Q_{zz}-Q_{yy})$	$-iQ_{xy}$	iQ_{xz}	0	$2iQ_{yz}$	$-2iQ_{yz}$
S_y		iS_x	iQ_{xy}	$i(Q_{xx}-Q_{zz})$	$-iQ_{yz}$	$-2iQ_{xz}$	0	$2iQ_{xz}$
S_z			$-iQ_{xz}$	iQ_{yz}	$i(Q_{yy}-Q_{xx})$	$2iQ_{xy}$	$-2iQ_{xy}$	0
Q_{yz}				$-iS_z$	iS_y	0	$-2iS_x$	$2iS_x$
Q_{xz}					$-iS_x$	$2iS_y$	0	$-2iS_y$
Q_{xy}						$-2iS_z$	$2iS_z$	0
Q_{xx}							0	0
Q_{yy}								0

$$\begin{cases} \langle 0,N,0|[\hat{S}_x,\hat{Q}_{yz}]|0,N,0\rangle = -2iN \longrightarrow \Delta S_x \Delta Q_{yz} \geq N \\ \langle 0,N,0|[\hat{S}_y,\hat{Q}_{xz}]|0,N,0\rangle = -2iN \longrightarrow \Delta S_y \Delta Q_{xz} \geq N \end{cases}$$

"Spin-nematic squeezed vacuum in a quantum gas,"

C. D. Hamley, C. S. Gerving, T. M. Hoang, E. M. Bookjans and M. S. Chapman, Nature Physics, 8, 305 (2012).

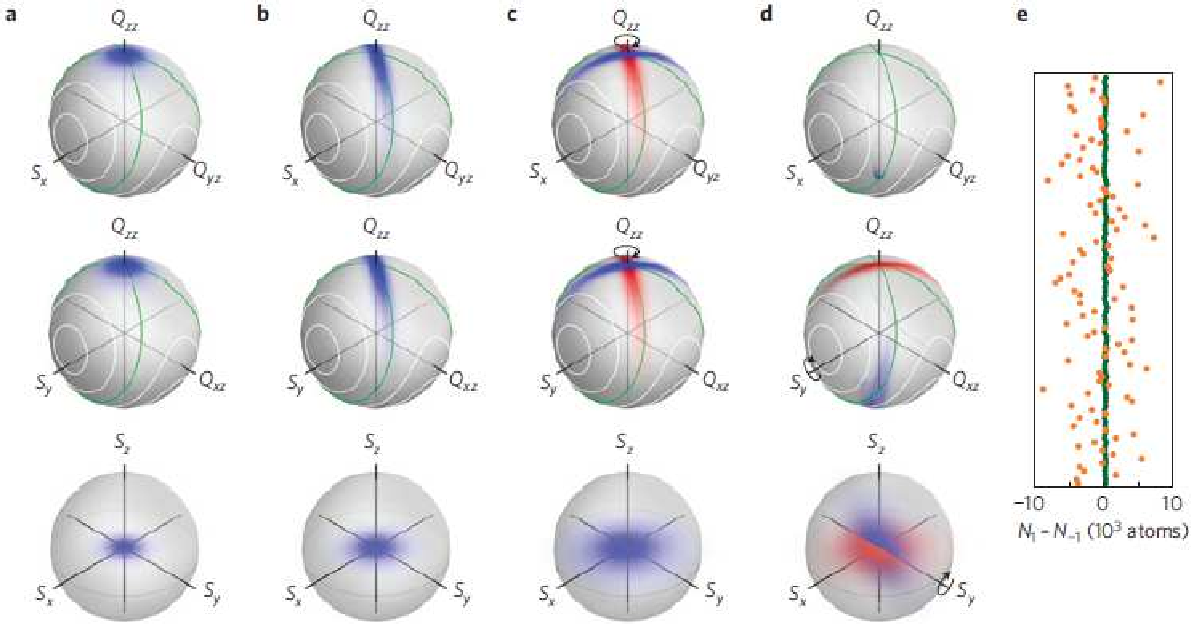

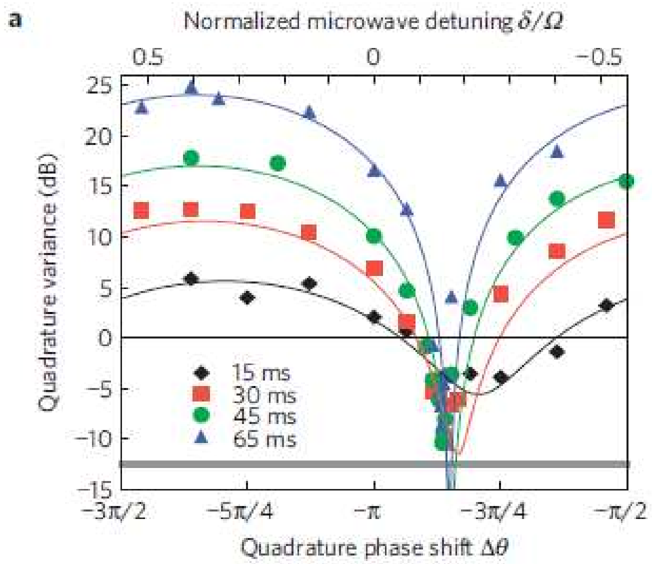

Figure 1 | Illustration of the experimental sequence using semi-classical simulation and quasi-probability distributions. a, The initial state is a condensate with the atoms prepared in the $m_f = 0$ state. An $N = 30$-atom distribution is used to emphasize features. **b**, After 25 ms of evolution, spin-nematic squeezing develops along the separatrix (green line) in the upper two spheres. **c**, A microwave pulse rotates the quadrature phase. For comparison the state from the previous plot is shown in red in the upper two spheres. **d**, A $\pi/2$ radiofrequency pulse rotates the transverse magnetization S_x into S_z. For comparison the state from the previous plot is shown in red in the lower two spheres. **e**, After the trap is turned off, a Stern–Gerlach field is applied during the time-of-flight expansion and the clouds of atoms are counted using fluorescence imaging. Measurements of $\langle S_z \rangle = N_1 - N_{-1}$ are shown for 100 runs of a squeezed quadrature (green) and an unsqueezed quadrature (orange).

Outline

1. Introduction
2. Magnetometer
3. Quantum enhanced measurements
4. Scaling
5. Conclusions

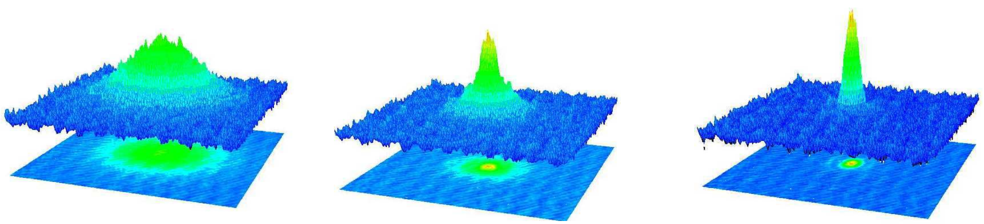

量子計測:スケーリング

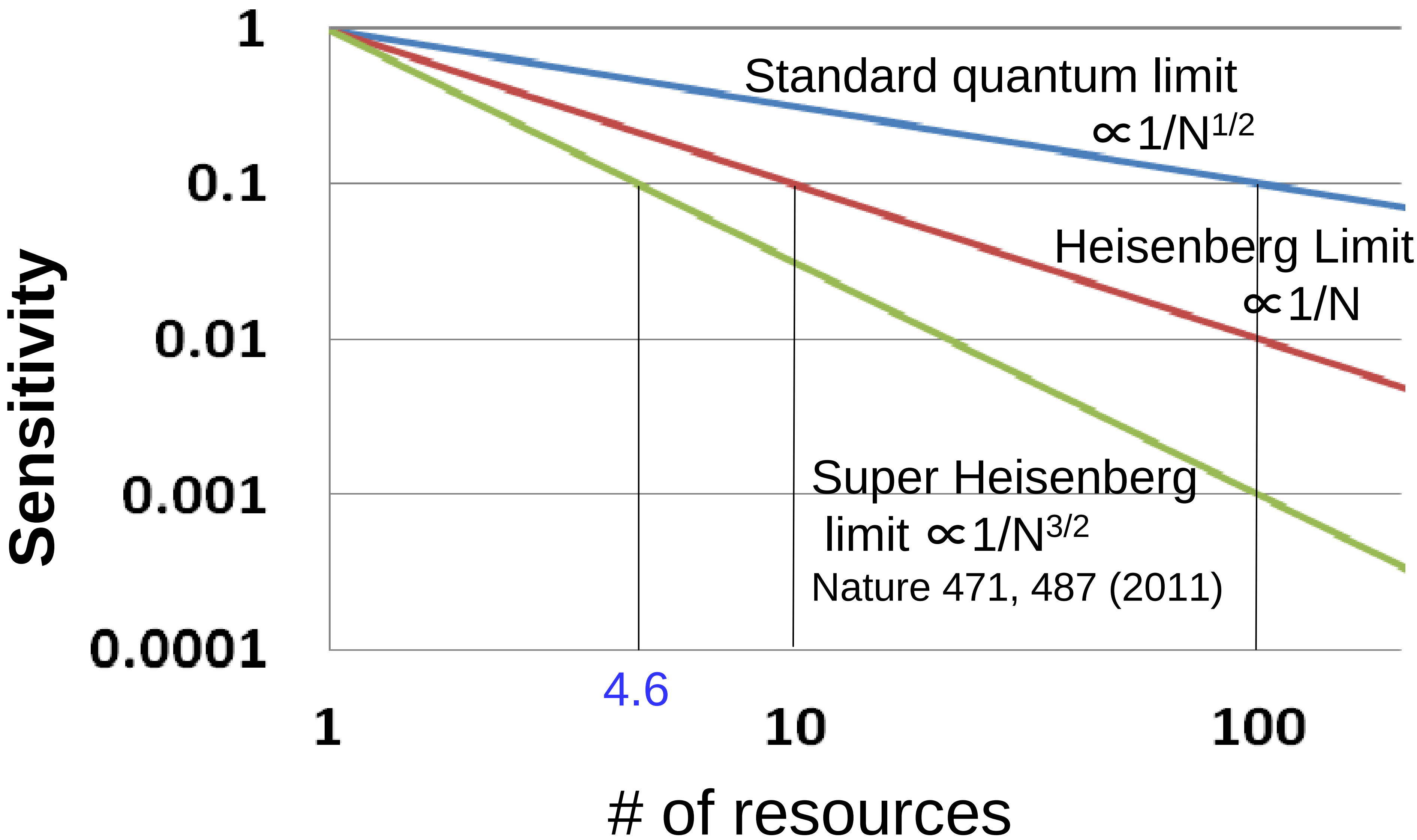
Sensitivity
1
0.1
0.01
0.001
0.0001
Standard quantum limit
∝1/N1/2
Heisenberg Limit
∝1/N
Super Heisenberg
limit ∝1/N3/2
Nature 471, 487 (2011)
4.6
1
10
100
# of resources

Example of SQL scaling : polarization rotation

全光子数をNとすると(ϕ<<1のとき)

垂直偏光　$N_{\perp}=N\sin^2(45+\phi)\approx N(1+2\phi)/2$

水平偏光　$N_{//}=N\cos^2(45+\phi)\approx N(1-2\phi)/2$

強度差をN_dとすると
$N_d=N_{\perp}-N_{//}=2N\phi$

$\Delta N_d=N^{1/2}$であるので

$\therefore \Delta\phi=\Delta N_d/(2N)$
$=1/(2N^{1/2})$

→標準量子限界のscaling

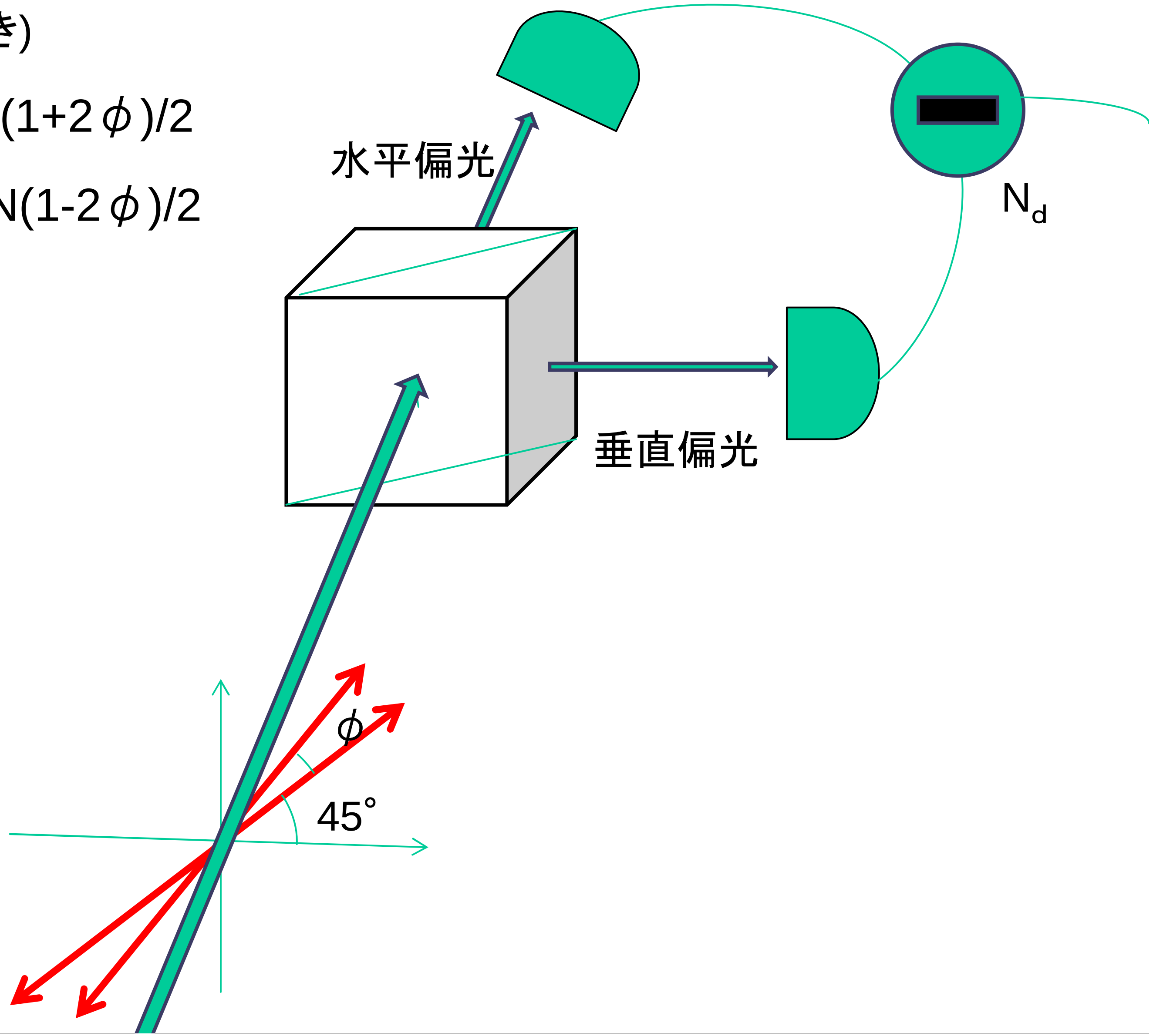

"Advances in quantum metrology,"
Vittorio Giovannetti, Seth Lloyd and Lorenzo Maccone, Nature Photonics, 5, 222 (2011).

Quantum estimation problem of recovering the value of a continuous parameter *x*

Quantum Cramér–Rao bound

$$\delta X_n \geqslant \min_{\rho_0^{(n)}} \left[\frac{1}{\sqrt{J(\rho_x^{(n)})}} \right] \quad , \quad J(\rho_x) = \mathrm{Tr}\left[R_{\rho_x}^{-1}(\rho_x')\rho_x R_{\rho_x}^{-1}(\rho_x') \right], \quad \rho_x' = \partial\rho_x / \partial x, \quad R_{\rho_x}^{-1}(O) = \sum_{j,k,\lambda_j+\lambda_j \neq 0} \left(\frac{2O_{jk}|j\rangle\langle k|}{(\lambda_j+\lambda_j)} \right)$$

Due to the additivity of the quantum Fisher information, for tensor states $J(\rho_x^{\otimes n}) = nJ(\rho_x) \longrightarrow$ SQL scaling

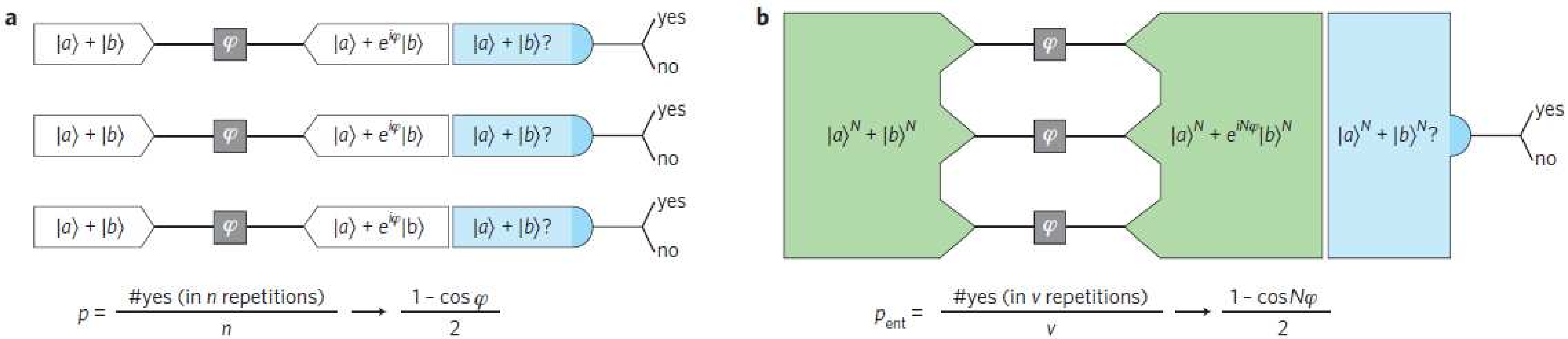

Figure 1 | Ramsey interferometry. The aim of Ramsey interferometry is to measure an unknown relative phase φ picked up by two orthogonal states ($|a\rangle$, $|b\rangle$) of an atomic probing system. This procedure can be generalized to other interferometric measurements such as frequency-standards, magnetometry and optical phase[2]. **a**, In a conventional set-up, 'probe preparation' consists of producing each atom in the superposition $|\Psi_{in}\rangle = (|a\rangle + |b\rangle)/\sqrt{2}$, which yields the output state $|\Psi_\varphi\rangle = (|a\rangle + e^{i\varphi}|b\rangle)/\sqrt{2}$ after the probing stage (shown as grey boxes). 'Readout' consists of checking whether $|\Psi_\varphi\rangle$ is still in the initial state $|\Psi_{in}\rangle$, which occurs with probability $p = |\langle\Psi_{in}|\Psi_\varphi\rangle|^2 = (1 - \cos\varphi)/2$. Thus, by taking the ratio between the number of successes and the total number of readouts, we can recover the phase φ. If we repeat this measurement n times, the associated error on our estimation of φ can then be evaluated using the standard deviation on the determination of p and by error propagation theory to obtain an SQL scaling of $n^{1/2}$. **b**, The quantum-enhanced case. A simple quantum strategy consists of dividing the n probes into groups of N, prepared in an entangled state $(|a\rangle^{\otimes N} + |b\rangle^{\otimes N})/\sqrt{2}$. Because each of the N vectors $|b\rangle$ acquires a relative phase φ, the final state is $(|a\rangle^{\otimes N} + e^{iN\varphi}|b\rangle^{\otimes N})/\sqrt{2}$. The probability that this state is equal to the initial one is now $p_{ent} = (1 - \cos N\varphi)/2$. Because we have $\nu = n/N$ groups of probes, we can repeat this procedure ν times with the same resources to obtain an error of $\delta\varphi_n = 1/\sqrt{(nN)}$, which is an $N^{1/2}$ increase in precision over the previous case, namely the Heisenberg bound, which scales as $1/(N\sqrt{\nu})$ (refs 3,4).

"Real-World Quantum Sensors: Evaluating Resources for Precision Measurement,"
Nicholas Thomas-Peter, Brian J. Smith, Animesh Datta, Lijian Zhang, Uwe Dorner, and Ian A. Walmsley, Phys. Rev. Lett. 107, 113603 (2011)

Quantum phenomena present in many experiments signify nonclassical behavior, but do not always imply superior performance. Quantifying the enhancement achieved from quantum behavior needs careful analysis of the resources involved. We analyze the case of parameter estimation using an optical interferometer, where increased precision can in principle be achieved using quantum probe states. Common performance measures are examined and some are shown to overestimate the improvement. For the simplest experimental case we compare the different measures and exhibit this overestimation explicitly. We give the preferred analysis of these experiments and calculate benchmark values for experimental parameters necessary to realize a precision enhancement. Our analysis shows that unambiguous real-world enhancements in optical quantum metrology with fixed photon number are yet to be attained.

A common practice is to "post-select" on particular measurement outcomes and neglect the occurrence of others, including when nothing is detected at the output. This amounts to setting η_p, η, η_d to 1 and $N = N_d$. This neglects both ν and the true N, significantly underestimating the exponentially growing number of trials [11] and information from neglected measurement outcomes.

"Magnetic Field Sensing Beyond the Standard Quantum Limit Using 10-Spin NOON States," Jonathan A. Jones, Steven D. Karlen, Joseph Fitzsimons, Arzhang Ardavan, Simon C. Benjamin, G. Andrew D. Briggs, John J. L. Morton, Science, 324, 1166 (2009).

TMP: trimethyl phosphite
The B spins cannot be distinguished.

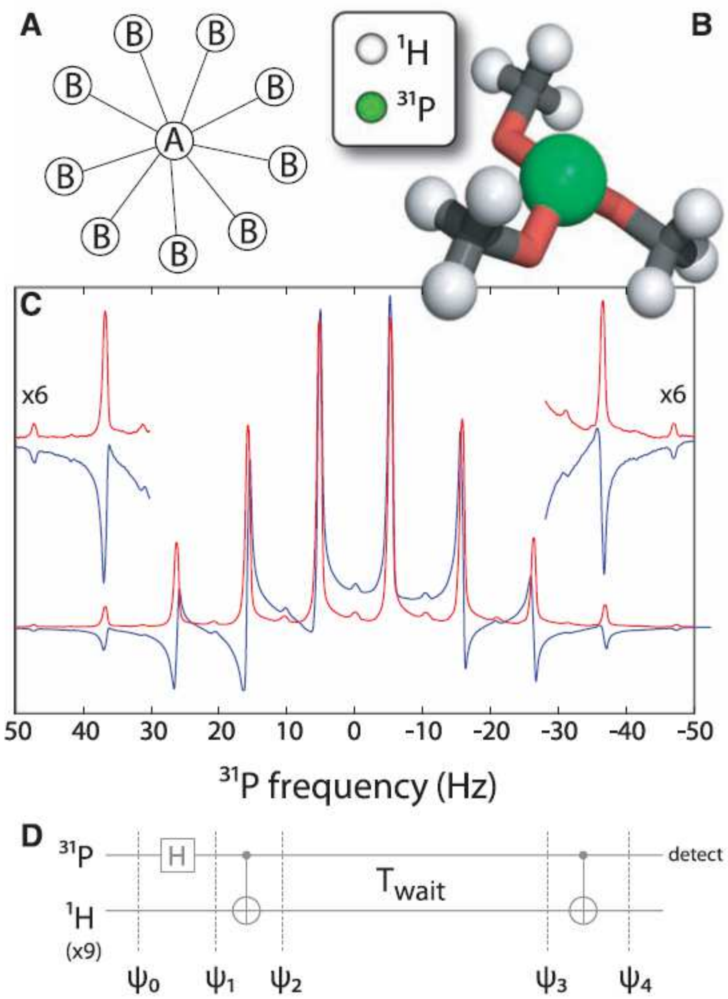

Fig. 1. Ten-spin NOON states are created by using nuclear spins in the TMP molecule. (**A**) Topology of the spin qubits used to generate the spin-NOON state. (**B**) The TMP molecule consists of a central ^{31}P nuclear spin surrounded by nine identical ^{1}H spins. (**C**) The initial ^{31}P NMR spectrum of TMP (red). Nuclear spin-NOON and MSSM states are generated and allowed to evolve for some short time under the influence of an off-resonance magnetic field. After mapping these entangled states back to the ^{31}P, the resulting spectrum (blue) shows how the phase shift acquired increases with the lopsidedness of the state. Low-intensity peaks between pairs of NMR lines arise from coupling to impurities. (**D**) Spin-NOON states are generated by first applying a Hadamard gate to the ^{31}P followed by a C-NOT on the nine equivalent ^{1}H.

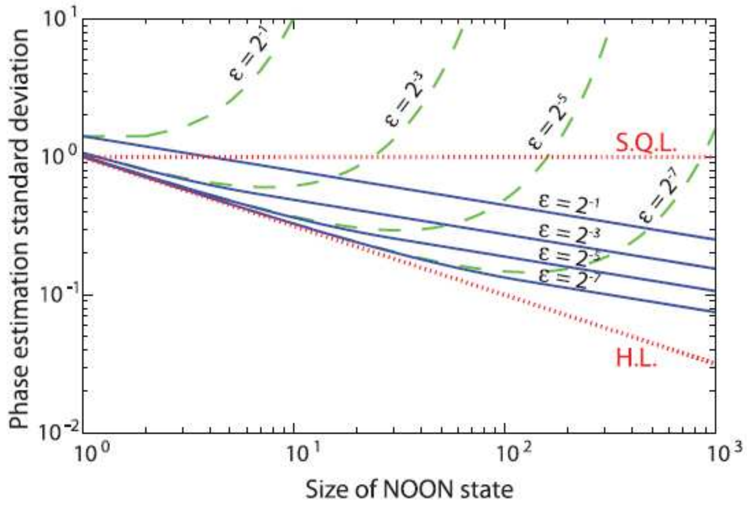

Fig. 3. Spin-NOON states exhibit an enhanced robustness to noise as compared with optical NOON states. Shown is a comparison of the effect of noise on the SD of phase estimates for spin-NOON (blue solid curves) and optical NOON states (green dashed curves) for a range of error probabilities. For photonic systems, the dominant source of error is taken to be photon loss, which is assumed to occur with probability ε. For spin-NOON states, the dominant source of error is taken to be a set of random normally distributed magnetic fields that lead to the complete dephasing of disentangled spins with probability ε over the time scale of the measurement. The upper and lower dotted lines indicate the standard quantum limit and the Heisenberg limit, respectively. The contribution is plotted per spin/photon, rather than per NOON state, in order to allow a direct comparison of states of varying size.

"Interaction-based quantum metrology showing scaling beyond the Heisenberg limit,"
M. Napolitano, M. Koschorreck, B. Dubost, N. Behbood, R. J. Sewell & M. W. Mitchel, Nature 471, 486 (2011).

nonlinear
Faraday rotation
probe pulses
Interaction
between probes

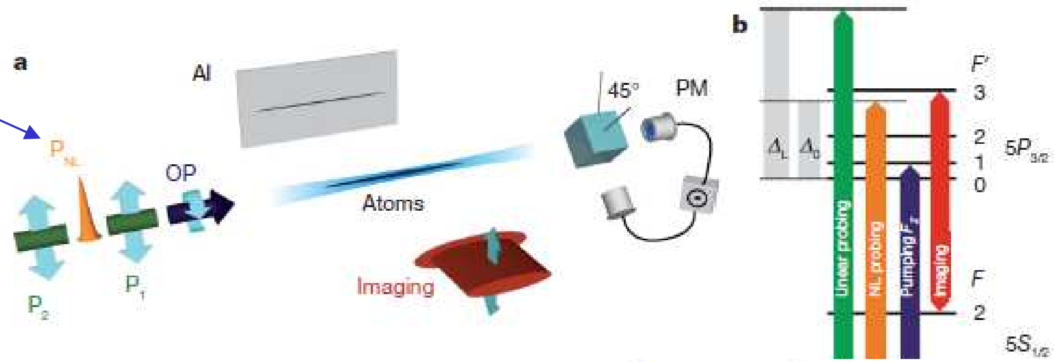

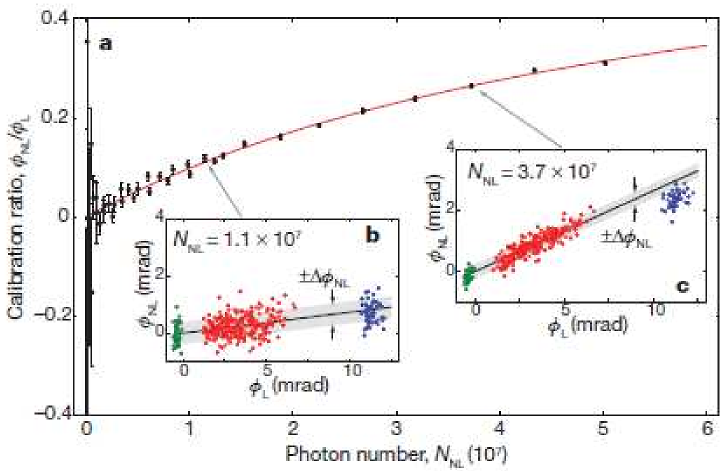

Figure 2 | **Calibration of nonlinear Faraday rotation.** **a**, Ratio of the nonlinear rotation, ϕ_{NL}, to the linear rotation, ϕ_L, versus the nonlinear probe photon number, N_{NL}. The data points and error bars indicate best-fit and standard errors from a linear regression, $\phi_{NL} = b\phi_L + \text{const.}$, for given values of N_{NL}. The red curve is a fit using equation (2), showing the expected nonlinear behaviour, $\phi_{NL} \propto N_{NL}$, with some saturation for large values of N_{NL}. **b**, **c**, ϕ_L-vs-ϕ_{NL} correlation plots for two values of N_{NL}. The atom number, N_A, is varied to produce a range of ϕ_L and ϕ_{NL} values. Green, no atoms ($N_A = 0$); red, $1.5 \times 10^5 < N_A < 3.5 \times 10^5$; blue, $N_A \approx 7 \times 10^5$. The blue circles are shown as a check on detector saturation, and are not included in the analysis.

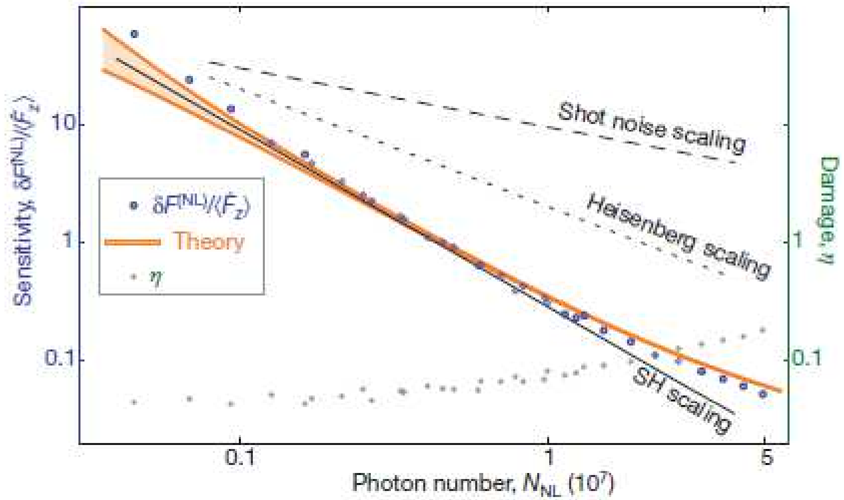

Figure 3 | **Super-Heisenberg scaling.** Fractional sensitivity, $\delta F_z^{(NL)}/\langle \hat{F}_z \rangle$, of the nonlinear probe plotted versus the number of interacting photons, N_{NL}. Blue circles indicate the measured sensitivity, orange curves show results of numerical modelling, and the black lines indicate SQL, Heisenberg-limit and super-Heisenberg (SH) scaling for reference. Scaling surpassing the Heisenberg limit, $\propto N_{NL}^{-1}$, is observed over two orders of magnitude. The measured damage to the magnetization, η, shown as green circles, confirms the non-destructive nature of the measurement. Error bars for standard errors would be smaller than the symbols and are not shown.

Summary

- Quantum Measurements, Quantum Metrology, Quantum sensing

  Important and promising application of QIP technologies

- Quantum enhanced measurements in a real world

  GW detector, magnetometer, etc.

- Scaling

  SQL, HL, Super HL (and, exponential) scaling

- Enhancement by entangled qubits